
Politecnico di Torino


## Politecnico di Torino

### Department of Mechanical and Aerospace Engineering


Master of Science in
Aerospace and Astronautical Engineering
(LM-20)

# Shape sensing of sandwich beams based on the Refined Zigzag Theory and on the inverse Finite Element Method


Supervisor:
Marco Gherlone

Co-supervisor:
Marco Esposito

Candidate:
Federica Pierri
ID: s332185


a.a. 2025/2026

**Abstract**

Shape sensing is the inverse problem of reconstructing the displacement field of a structure from discrete strain measurements. From displacements, full-field strains and stresses can also be evaluated, enabling Structural Health Monitoring, the control of morphed structures, and the development of predictive maintenance strategies and Digital Twin technologies.
Among the various approaches proposed for shape sensing, the inverse Finite Element Method (iFEM) has emerged as particularly effective due to its versatility regarding complex loading conditions, material systems, and geometries. Based on the FEM discretization of the analyzed component and on the least-square compatibility between measured and reconstructed strains, iFEM has been initially formulated for thin-walled components, then extended to beam and frame structures and more recently to moderately thick multilayered plates.
This thesis develops a one-dimensional inverse element for the shape sensing of multilayered composite and sandwich beams. The formulation couples the iFEM technique and the Refined Zigzag Theory for multilayered structures. The performance of the proposed element is assessed through both numerical analyses and experimental tests on sandwich beams subjected to bending. Strains evaluated/measured on the external surfaces and at one of the facesheet-core interfaces serve as input data for the 1D inverse approach, while reference deflections evaluated/measured at key locations are used to numerically/experimentally validate the accuracy of the reconstruction. The thesis focuses on different approaches to deal with the compatibility between reconstructed and measured strains. In particular, an investigation on the importance of including transverse shear strain contributions is performed for different sandwich stacking sequences.

«Si parte!!!
Verso il "Nuovo Mondo"!!! »

— Monkey D. Luffy, One piece

*A mio padre e mia madre,*
*il mio esempio più grande.*

*Alle mie nipotine, Giorgia e Ginevra,*
*perché il vostro amore è la ricarica più potente*
*che io abbia mai conosciuto.*

*A Luisci, che ha saputo incoraggiare*
*i miei sogni.*

*A Pana, fonte di forza e di*
*ispirazione per me!*

# Table of Contents

# List of Tables

# List of Figures

# Chapter 1

# Introduction

The safety and integrity of primary components is the fundamental objective in the field of modern structural engineering, with a particular focus on the aerospace sector. In general, structural reliability has been managed by *Time-Based Maintenance* (TBM) protocols, which are based on scheduled inspections and the replacement of components at flight-hour intervals, often regardless of structural degradation. Sadly, this approach is inefficient and involves high operational costs, as it requires the grounding of aircraft that are still airworthy. In this scenario of continuous pursuit of efficiency, the transition toward **Structural Health Monitoring (SHM)** should not be viewed merely as a genuine strategic evolution and a paradigm shift toward **Condition-Based Maintenance (CBM)** [1]. This fundamental transition is realized through the integration of a complex and widespread network of sensors, which can be embedded directly within the material matrix or meticulously applied to the external surfaces of the components. In this configuration, SHM enables continuous detailed and above all real time observation of all kinematic and stress parameters considered critical for global stability. This technological leap, which aims to overcome the limitation of tradition diagnostics based on fixed intervals, finds its primary scientific and industrial motivation in a series of determining factors that directly impact the entire lifecycle of the aircraft:

- **Enhanced Safety**: the ability to identify early-stage damage that remains invisible to the naked eye, such as interlaminar delaminations or internal micro-crack, is vital for preempting catastrophic structural failures [2].
- **Cost Efficiency**: the ability to schedule maintanance interventions based on the actual state of structural degradation allows for the drastic reduction of unnecessary technical downtime. By minimizing redundant inspections and periods of forced aircraft inactivity, this approach ensures more efficient management of the structure's life cycle while significantly enhancing its operational longevity [1].

- **Design Optimization**: access to real-time data on operational loads and structural deformation responses is of paramount importance for designers, as it enables the refinement of safety margins with a higher degree of precision. This optimization leads to a direct reduction in the total weight of the aircraft and, consequently, to a significant decrease in fuel consumption [1].

## 1.1 Sandwich structures

Within this framework of structural optimization, sandwich configurations play a vital role. Their efficiency stems from exceptional stiffness-to-wight ratio, achieved by bonding two thin, rigid facesheet to lightweight, compliant core [1]. The selection of materials is fundamental to fully exploiting this synergy: the facesheets, which bear the bending loads, are typically manufactured from high-strength materials such as **aluminum alloys** or **fiber-reinforced composites** (carbon, glass or aramid). Conversely, the core is designed to withstand transverse shear loads and is usually composed of ultra-lightweight materials, including metallic or non-metallic honeycombs, balsa wood or open and closed-cell synthetic foams. [3]

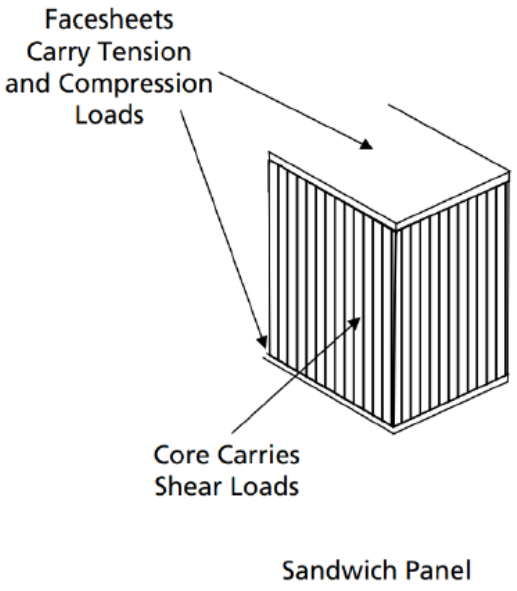


**Figure 1.1:** Schematic representation of a sandwich panel [3]

Combining facesheets and core allows the sandwich panel to possess high mechanical characteristics and stiffness, even though the core materials may appear fragile when taken alone. Thanks to this particular aspect, sandwich materials are used

in aerospace applications such as **panels and fuselage structure**, where the primary requirement is indeed maximum structural efficiency. [1]

## 1.2 Kinematic Modeling: From Classical Theories to RZT

As seen in the previous paragraph, sandwich configurations offer important structural advantages, and the fact that they are composed of different materials introduces extremely significant modeling challenges, giving rise to what are known as **complicating effects of layered structures**. The isotropic single-layer exhibit uniform properties, whereas sandwich structures are characterized by:

- **in-plane anisotropy**: the structure possesses different mechanical and physical properties in various directions within the plane. This results in the coupling between shear and logitudinal strains, which introduces significant complexities into the solution procedure for anisotropic structures. [4]
- **transverse anisotropy**: mechanical and physical properties change abruptly along the thickness direction $z$ at each interface between the facesheets and the core.[4]

A classical approach for multi-layered structures is the **First-order Shear Deformation Theory (FSDT)**, which is based on the assumption that displacements vary linearly and continuously through the thickness. Furthermore, FSDT is based on the hypothesis that a cross-section, initially plane and orthogonal to the longitudinal axis, remains plane but not necessarily orthogonal after deformation, consequently the transverse shear strain distribution is constant.
The specific behavior of multi-layered structures imposes the fulfillment of the $C_z^0$ requirements (Interlaminar Continuity). [1]

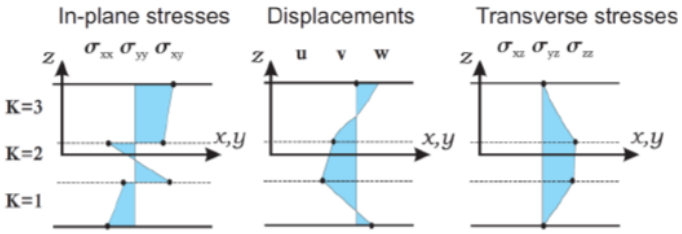


**Figure 1.2:** $C_z^0$ requirements (Interlaminar Continuity) [4]

Under these requirements, displacements must remain continuous in the $z$-direction for reason of **kinematic congruency**, while transverse shear and normal stresses

must be continuous through the thickness to satisfy **equilibrium** conditions. Moreover, the first derivatives of displacements and transverse stresses are discontinuous because the mechanical properties change abruptly in each layer; this phenomenon is precisely what gives rise to the **zigzag (ZZ) effect**. [2]
In general, 2D theories must account for these effects, yet they are often insufficient. For this reason, it is necessary to adopt a more refined approach, such as the **Refined Zigzag Theory (RZT)**. RZT enriches the displacement field with a piecewise-linear zigzag function, allowing it to satisfy the $C_z^0$ requirements while maintaining the computational efficiency typical of 2D formulations. While full **layer-wise** model, which treat each individual ply ad an independent structural entity, ensure high precision, they are often computationally prohibitive. Therefore, this theory, by enriching the kinematic field with a piecewise-linear function that satisfies the $C_z^0$ requirements, represents an excellent alternative because it has a low computational cost. Following the robust formulation proposed by [1], the axial displacement $u_x$ is defined as:

$$u_x(x, z) = u(x) + z\theta(x) + \phi(z)\psi(x) \tag{1.1}$$

In this framework:

- $u(x)$: uniform translation of the mid-plane.
- $z\theta(x)$: global rotation of the cross-section.
- $\phi(z)\psi(x)$: it is a corrective term. $\phi(z)$ is a predefined zigzag function that dictates the geometric shape of the distortion through the thickness, while $\psi(x)$ governs its spatial amplitude along the longitudinal axis of the beam.

Using this approach means reconstructing a stress state that is physically consistent and continuous across material interfaces. For a **structural health monitoring system**, this precision is essential to capture localized stress gradients with the necessary accuracy, as these often warn of structural failure. [2]

## 1.3 The iFEM methodology: bridging sensing and structural reconstruction

The concepts discussed above are implemented into a practical engineering tool known as the **INVERSE FINITE ELEMENT METHOD (iFEM)**. This approach represents a significant departure from direct structural analysis; while the latter requires precise knowledge of external loads and material properties, which are often unknown or stochastic during fight, iFEM operates solely on kinematic data provided by a discrete network of sensors. Since this method does

not require prior knowledge of external loading conditions, it is exceptionally robust for real-time aerospace applications. [2]
Given that the subsequent discussion will focus on sandwich beams modeled according to the **Refined Zigzag Theory (RZT)** [5], it is worth anticipating that the cross-sectional kinematics will be described by specific generalized strain components:

- $\epsilon$: membrane strain.
- $\kappa$: bending curvature.
- $\mu$: denotes the bending strain measure related to the zigzag effect (the RZT kinematic enrichment).
- $\eta^{\epsilon}$ and $\gamma^{\epsilon}$: represent the zigzag transverse shear strain measure and average transverse shear strain measure.

However, to fully understand the mathematical logic underlying the *iFEM* algorithm before introducing the *RZT* formulation, it is useful to illustrate the construction of the error functional according to the kinematic assumptions of the *Eulero-Bernoulli* theory [6].
Considering a $1D$ reference system where $x$ is the longitudinal axis and $z$ is the transverse axis (thickness direction), the kinematic displacement field is expressed as [6]:

$$\begin{cases} u_x = u - z \cdot w_{,x} \\ u_z = w \end{cases} \tag{1.2}$$

where $u$ and $w$ are respectively the axial and transverse displacements of the reference axis, and $w_{,x}$ denotes the first derivative of the transverse displacement with respect to the coordinate $x$.
By differentiating the displacement field, and introducing the analytical definitions of the membrane strain $\epsilon = u_{,x}$ and the bending curvature $\kappa = -w_{,xx}$, the axial strain of the cross-section can be rewritten in the compact form [6]:

$$\epsilon_{xx} = \epsilon + z \cdot \kappa \tag{1.3}$$

The core of the *iFEM* method consists of minimizing a least-squares error functional. For a single inverse finite element discretized with $N$ measurement points, the functional $\Phi$ is written ad the sum of squared errors for the strains [6]:

$$\Phi = \sum_{k=1}^{N} (u_{,x} - \epsilon^{\epsilon})^2 + \sum_{k=1}^{N} (-w_{,xx} - \kappa^{\epsilon})^2 \tag{1.4}$$

where:

- $u_{,x}$ and $-w_{,xx}$ are analytical quantities
- $\epsilon^{\epsilon}$ and $\kappa^{\epsilon}$ represent the corresponding experimental strain measurements acquired by the physical sensors.

By showing this simple sum of two quadratic terms, it becomes immediate to understand the basic architecture of the method. Moving from the didactic Eulero-Beroulli model to the advanced formulation necessary to accurately model composite and sandwich structures, the present work adopts the **Refined Zigzag Theory (RZT)** applied to beams [5]. In the framework of the *RZT*, the kinematics is enriched to realistically describe the zigzag distortion of the layers and the shear strains.
Consequently, the error functional will maintain the same least-squares structure, but will naturally contain more terms in order to couple the experimental data with the entire set of generalized kinematic components ($\epsilon$, $\kappa$, $\mu$, $\phi$, $\eta$).
By integrating the internal stresses along the thickness of the laminate, the stress resultants (generalized forces and moments) are defined. The macroscopic constitutive relations linking these resultants to the previously defined strain components are expressed through the cross-sectional stiffness matrices [5]. For the axial, bending and zigzag behavior, the matrix relationship is as follow:

$$\begin{Bmatrix} N_x \\ M_x \\ M_\phi \end{Bmatrix} = \begin{bmatrix} A_{11} & B_{11} & C_{11} \\ B_{11} & D_{11} & E_{11} \\ C_{11} & E_{11} & F_{11} \end{bmatrix} \begin{Bmatrix} \epsilon \\ \kappa \\ \mu \end{Bmatrix} \tag{1.5}$$

where $N_x$ represents the normal force, $M_x$ the global bending moment and $M_\phi$ the generalized zigzag moment. The terms of the matrix (from $A_{11}$ to $F_{11}$) indicate the membrane, bending and relative coupling stiffness coefficients.
Similarly, the constitutive relation governing the transverse shear behavior is defined as [5]:

$$\begin{Bmatrix} V_x \\ V_\phi \end{Bmatrix} = \begin{bmatrix} A_{44} & B_{44} \\ C_{44} & D_{44} \end{bmatrix} \begin{Bmatrix} \theta + w_{,x} \\ \phi \end{Bmatrix} \tag{1.6}$$

where $V_x$ is the conventional transverse shear force and $V_\phi$ is the generalized zigzag shear force, while the coefficients from $A_{44}$ to $D_{44}$ constitute the transverse shear stiffnesses of the cross-section.
Starting from these constitutive relations and applying the *Principle of Virtual Work*, it is possible to derive the equilibrium equations [5]. This theoretical derivation is crucial importance for the *iFEM* algorithm. In fact, the $e = 1$ which includes the equilibrium equations are exploited to analytically express the unknown zigzag transverse shear ($\eta$) and average transverse shear strain ($\gamma$), solely as a functional of the derivatives of the ($\epsilon$, $\kappa$, $\mu$). This sophisticated mathematical step allows the

*iFEM* method to capture the shear deformability of sandwich structures without requiring any complex and impractical direct measurement of shear in the field. By substituting the constitutive relations into the equilibrium equations, the following resolving system is obtained:

$$\begin{cases} B_{11}\epsilon_{,x} + D_{11}\kappa_{,x} + E_{11}\mu_{,x} = (A_{44} + B_{44})\gamma^{\epsilon} - B_{44}\eta^{\epsilon} \\ C_{11}\epsilon_{,x} + E_{11}\kappa_{,x} + F_{11}\mu_{,x} = (C_{44} + D_{44})\gamma^{\epsilon} - D_{44}\eta^{\epsilon} \end{cases} \tag{1.7}$$

## 1.4 Thesis objectives

The thesis seeks to bridge two distinct fields: the kinematic precision of the **Refined Zigzag Theory (RZT)** and the versality of the **inverse Finite Element Method (iFEM)**, applying them specifically to sandwich beam elements. Developed entirely within a **MATLAB** framework, the code is designed to overcome the structural hurdles inherent in classical theories, specifically their struggle to accurately reconstruct interminar states.
It is therefore necessary to define the governing equations of the inverse beam element, integrating the equilibrium equations within the *MATLAB* environment. Two distinct approaches are analyzed:

- **e=0**: the formulation in which equilibrium equations are not implemented. This reflects the original iFEM-RZT approach proposed by Cerracchio [2]
- **e=1**: the formulation that includes the enforcement of structural equilibrium equations. This follows the advanced methodology established by Kefal [1], in which the least-squares functional is enriched by satisfying the RZT equilibrium equations to improve the accuracy of deflection and transverse shear stress prediction.

Once the code is established, the entire framework is validated through a comparison with a direct model within the *MATLAB* environment. The robustness of the numerical framework is then validated through a rigorous comparison with high-fidelity solutions obtained using the commercial software **Patran**, a crucial step to certify the accuracy of the iFEM-RZT model in complex operational scenarios. Finally, the entire methodology finds its definitive confirmation through comparison with real experimental data acquired in the laboratory, demonstrating the effectiveness of the approach in translating discrete sensor measurements into an accurate physically consistent mapping of structural health.

# Chapter 2

# Inverse finite element formulation for sandwich beams

As conceptually introduced in the previous chapter, the core of the structural monitoring procedure lies in the definition of a weighted least-squares functional $\Phi$. For a single element of length $L$, this functional is constructed as the sum of five integral contributions, where each term represents the squared difference between an analytical quantity and the corresponding experimental measurement obtained from the sensors.
The fundamental logic of this approach is to enforce the derivatives of the analytical displacements to match the experimental strain gradients. By minimizing this discrepancy, the algorithm determines the optimal distribution of the kinematic field $\mathbf{u}$ over the entire element.

$$\begin{aligned}\Phi(\mathbf{u}) =& \frac{1}{2}\int_0^L \left[u_{,x} - \epsilon^\epsilon\right]^2 dx + \frac{A}{2}\int_0^L \left[\theta_{,x} - \kappa^\epsilon\right]^2 dx + \frac{A}{2}\int_0^L \left[\psi_{,x} - \mu^\epsilon\right]^2 dx + \\ & \frac{1}{2}[e + (1-e)\alpha]\int_0^L \left[(w_{,x} + \theta - \psi) - e\eta^\epsilon\right]^2 dx + \frac{1}{2}e\int_0^L \left[(w_{,x} + \theta) - \gamma^\epsilon\right]^2 dx\end{aligned} \tag{2.1}$$

Within the functional, $A$ represents the cross-sectional area of beam, while $\alpha$ is a penalty parameter used to constrain the transverse shear terms. The quantities $\epsilon^\epsilon, \kappa^\epsilon, \mu^\epsilon, \gamma^\epsilon$ and $\eta^\epsilon$ represent the targets of the generalized kinematic components of the $RZT$ beam, whose physical definitions were already extensively discussed in the previous chapter. It should be noted that the first terms $(\epsilon^\epsilon, \kappa^\epsilon, \mu^\epsilon)$ can be determined directly via surface strain sensors, allowing for the reconstruction of $u$, $\theta$ and $\phi$. However, these measurements alone are insufficient to uniquely

determine the transverse deflection $w$. Since transverse shear strains cannot be easily measured using surface sensors, the algorithm exploits the multiplicative parameter $e$ to handle this limitation. Consistent with the previously introduced theoretical framework, the parameter $e$ defines the nature of the solution:

- when $e = 0$, the formulation does not use equilibrium equations or material properties. In this purely kinematic approach, the penalty parameter $\alpha$ is employed to enforce the condition $\eta \approx 0$. It is crucial to specify that this constraint is applied exclusively to the zigzag component $\eta$, while the average transverse shear strain $\gamma$ is completely excluded from the calculation. This provides the necessary kinematic link to uniquely resolve the transverse deflection $w$ using only surface data.
- when $e = 1$, the structural model incorporates the cross-sectional equilibrium equations and the specific constitutive characteristics to analytically derive the shear strain $(\gamma^\epsilon, \eta^\epsilon)$. This allows for a physically rigorous and completely autonomous reconstruction of both average transverse and zigzag transverse shear strain.

## 2.1 Finite element discretization and shape functions

The minimization of the error functional is performed at the element level, with integration limits ranging from 0 to element length $L$. This approach ensures that the minimization of local errors leads to the minimum global error for the assembled structure. The reference element is a two-node beam element, characterized by four degrees of freedom per node:

$$\{q\}_i = \{u_i, w_i, \theta_i, \psi_i\}^T \quad (i = 1,2) \tag{2.2}$$

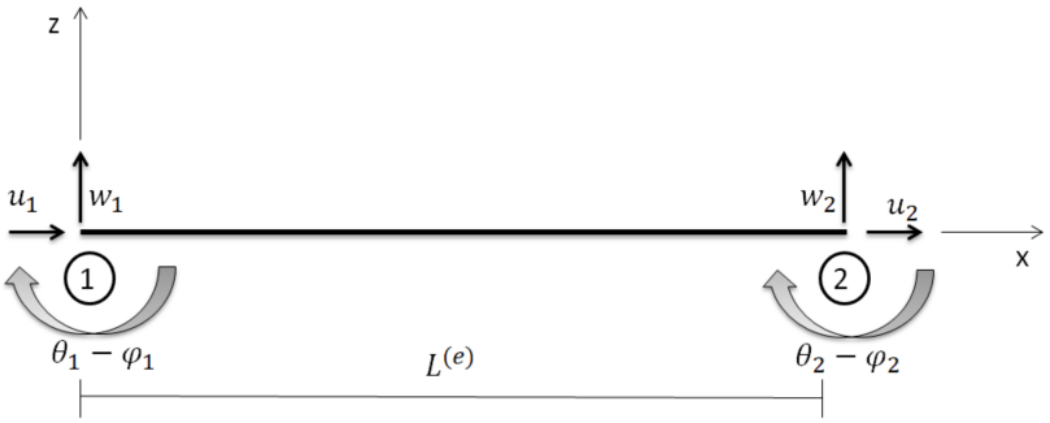


**Figure 2.1:** Nodal degrees of freedom and kinematic variables for the two-node RZT beam element.

To ensure kinematic consistency and avoid the well-known phenomenon of shear locking, the methodological framework for selecting the shape functions and interpolation strictly refers to the formulation of $C^0$ beam elements developed by [7] based on the $RZT$. For axial displacement $u$, rotation $\theta$ and zigzag function $\phi$, standard linear Lagrange shape functions are employed:

$$\begin{aligned} u &= L_1 u_1 + L_2 u_2 \\ \theta &= L_1 \theta_1 + L_2 \theta_2 \\ \psi &= L_1 \psi_1 + L_2 \psi_2 \end{aligned} \tag{2.3}$$

where $L_1$ and $L_2$ are defined as:

$$L_1 = 1 - \frac{x}{L}, \quad L_2 = \frac{x}{L} \tag{2.4}$$

To prevent shear locking, the transverse deflection $w$ requires a higher-order interpolation using an anisoparametric formulation [7]:

$$w = L_1 w_1 + L_2 w_2 + \frac{L}{8} p_m \left[ (\theta_2 + c\psi_2) - (\theta_1 + c\psi_1) \right] \tag{2.5}$$

In this expression, $p_m$ is a parabolic polynomial that vanishes at the nodes and equals unity at the element mid-span:

$$p_m = -4 \left( \frac{x}{L} \right)^2 + 4 \left( \frac{x}{L} \right) \tag{2.6}$$

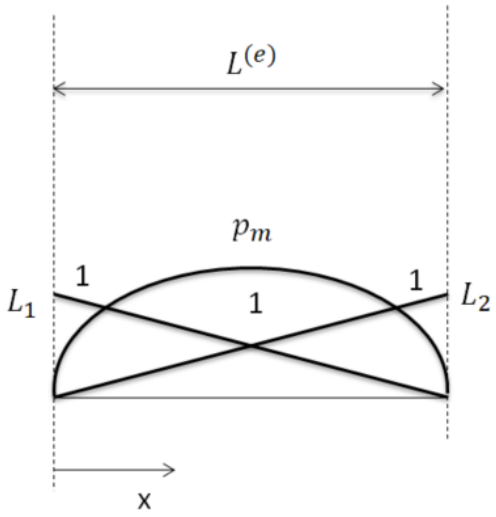


**Figure 2.2:** Inverse element

The introduction of the coefficient $c$ in the interpolation of $w$ is the key mathematical tool to enforce a specific shear-related quantity to remain constant along the element. The definition of this parameter (and consequently of the constrained quantity) strictly depends on the approach adopted for the shear calculation [7]:

- In the $\mathbf{e = 1}$ case, integrating the actual material properties through the equilibrium equations, the coefficient is defined by the section's shear stiffness ratio: $c = B_{44L}/A_{44L}$ This choice ensures that the quantity constrained to remain constant along the element is the **transverse shear force** ($V_x$), thus guaranteeing maximum physical adherence to the RZT theoretical model [7].
- In the $\mathbf{e = 0}$ case, the formulation is independent of the material data. To maintain a high level of accuracy and avoid purely kinematic numerical instability, the element requires the **zigzag transverse shear** $\eta$ to remain constant within the element. This condition is obtained analytically by setting $\mathbf{c = -1}$ [7].

## 2.2 Development of functional terms

In this section, the terms of the functional are developed separately.

### 2.2.1 Membrane strain ($u$)

The first term of the functional represents the membrane strain contribution. In a continuous formulation, this would require the knowledge of the strain field throughout the entire element. However, since experimental data are only available at specific locations where sensors are placed, the integral is replaced by a discrete summation over these measurement points:

$$\Phi_u = \frac{1}{2}\int_0^L [u_{,x} - \epsilon^\epsilon]^2\, dx \approx \frac{1}{2}\sum_{i=1}^{n} [u_{,x}(x_i) - \epsilon_i^\epsilon]^2 \tag{2.7}$$

The axial displacement $u(x)$ is expressed through the linear shape functions $L_1$ and $L_2$ and the nodal degrees of freedom (DoFs) vector $\mathbf{q}$:

$$u = \begin{bmatrix} L_1 & 0 & 0 & 0 & L_2 & 0 & 0 & 0 \end{bmatrix} \{q\} \tag{2.8}$$

where the vector $\{q\}$ collects the 8 degrees of freedom of the two-node element:

$$\{q\}^T = \{u_1, w_1, \theta_1, \psi_1, u_2, w_2, \theta_2, \psi_2\}^T \tag{2.9}$$

The derivative of $u$ with respect to $x$ is obtained by differentiating the shape functions, defining the $[B_u]$ matrix for the membrane term:

$$u_{,x} = [L_{1,x}\ 0\ 0\ 0\ L_{2,x}\ 0\ 0\ 0]\{q\} = [B_u]\{q\} \tag{2.10}$$

To develop the functional, the transposed form of the analytical strain is used:

$$u_{,x}^T = \{q\}^T [B_u]^T \tag{2.11}$$

Substituting the discretization into the membrane term of the functional, we obtain:

$$\Phi_u = \frac{1}{2}\sum_{i=1}^{n} (u_{,xi} - \epsilon_i^\epsilon)^T (u_{,xi} - \epsilon_i^\epsilon) \tag{2.12}$$

By substituting the kinematic relation into Eq. (2.11) and (2.12), the expression becomes:

$$\Phi_u = \frac{1}{2}\sum_{i=1}^{n} \left(\{q\}^T [B_{ui}]^T - \epsilon_i^\epsilon\right) ([B_{ui}]\{q\} - \epsilon_i^\epsilon) \tag{2.13}$$

Expanding the product within the summation:

$$\Phi_u = \frac{1}{2}\sum_{i=1}^{n}\left(\{q\}^T[B_{ui}]^T[B_{ui}]\{q\} + (\epsilon_i^\epsilon)^2 - 2\{q\}^T[B_{ui}]^T\epsilon_i^\epsilon\right) \tag{2.14}$$

Using the property of linearity, the summation can be split into three distinct terms:

$$\Phi_u = \frac{1}{2}\sum_{i=1}^{n}\left(\{q\}^T[B_{ui}]^T[B_{ui}]\{q\}\right) - \sum_{i=1}^{n}\left(\{q\}^T[B_{ui}]^T\epsilon_i^\epsilon\right) + \frac{1}{2}\sum_{i=1}^{n}(\epsilon_i^\epsilon)^2 \tag{2.15}$$

By factoring out the nodal degrees of freedom vector $\{q\}$, which does not depend on the summation index $i$, we obtain the final discretized form:

$$\Phi_u = \frac{1}{2}\{q\}^T\left(\sum_{i=1}^{n}[B_{ui}]^T[B_{ui}]\right)\{q\} - \{q\}^T\left(\sum_{i=1}^{n}[B_{ui}]^T\epsilon_i^\epsilon\right) + \frac{1}{2}\sum_{i=1}^{n}(\epsilon_i^\epsilon)^2 \tag{2.16}$$

At this stage, the following matrices are identified:

$$[A_u] = \sum_{i=1}^{n}[B_{ui}]^T[B_{ui}] \tag{2.17}$$

$$\{b_u\} = \sum_{i=1}^{n}[B_{ui}]^T\epsilon_i^\epsilon \tag{2.18}$$

Thus, the membrane contribution to the functional is simplified as follows:

$$\Phi_u = \frac{1}{2}\{q\}^T[A_u]\{q\} - \{q\}^T\{b_u\} + C \tag{2.19}$$

where $C$ is a constant term independent of the nodal displacements. The discretized functional is minimized with respect to the nodal degrees of freedom. By taking the partial derivative of $\Phi_u$ with respect to the vector $\{q\}$ and setting it to zero, the following relation is obtained:

$$\frac{\partial\Phi_u}{\partial\{q\}} = [A_u]\{q\} - \{b_u\} = 0 \tag{2.20}$$

Consequently, the resolving system for the membrane component is defined as:

$$[A_u]\{q\} = \{b_u\} \tag{2.21}$$

This linear system allows for the reconstruction of the nodal displacements based on the experimental strain data provided by the sensors.

### 2.2.2 Bending contribution ($\kappa$)

The second term of the functional, representing the bending contribution, is developed as follows:

$$\Phi_k = \frac{A}{2}\int_0^L \left[\theta_{,x} - \kappa^\epsilon\right]^2 dx \approx \frac{A}{2}\sum_{i=1}^{n}\left[\theta_{,xi} - \kappa_i^\epsilon\right]^2 \tag{2.22}$$

The rotation $\theta$ is interpolated using the linear shape functions $L_1$ and $L_2$:

$$\theta = [0\ 0\ L_1\ 0\ 0\ 0\ L_2\ 0]\{q\} \tag{2.23}$$

where the nodal degrees of freedom vector $\{q\}$ for the two-node element is defined as:

$$\{q\} = \{u_1, w_1, \theta_1, \psi_1, u_2, w_2, \theta_2, \psi_2\}^T \tag{2.24}$$

The analytical curvature $\theta_{,x}$ is obtained by differentiating the shape functions, defining the $[B_\theta]$ matrix:

$$\theta_{,x} = [0\ 0\ L_{1,x}\ 0\ 0\ 0\ L_{2,x}\ 0]\{q\} = [B_\theta]\{q\} \tag{2.25}$$

For the development of the functional, the transposed form of the analytical curvature is used:

$$\theta_{,x}^T = \{q\}^T[B_\theta]^T \tag{2.26}$$

Substituting the discretization into the bending term of the functional leads to:

$$\Phi_\theta = \frac{A}{2}\sum_{i=1}^{n}\left(\theta_{,xi} - \kappa_i^\epsilon\right)^T\left(\theta_{,xi} - \kappa_i^\epsilon\right) \tag{2.27}$$

By substituting the kinematic relation into Eq. (2.26), the expression becomes:

$$\Phi_\theta = \frac{A}{2}\sum_{i=1}^{n}\left(\{q\}^T[B_{\theta i}]^T - \kappa_i^\epsilon\right)\left([B_{\theta i}]\{q\} - \kappa_i^\epsilon\right) \tag{2.28}$$

Expanding the product within the summation yields:

$$\Phi_\theta = \frac{A}{2}\sum_{i=1}^{n}\left(\{q\}^T[B_{\theta i}]^T[B_{\theta i}]\{q\} + (\kappa_i^\epsilon)^2 - 2\{q\}^T[B_{\theta i}]^T\kappa_i^\epsilon\right) \tag{2.29}$$

Through the property of linearity, the summation is split into three distinct terms:

$$\Phi_\theta = \frac{1}{2}\{q\}^T\left(A\sum_{i=1}^{n}[B_{\theta i}]^T[B_{\theta i}]\right)\{q\} - \{q\}^T\left(A\sum_{i=1}^{n}[B_{\theta i}]^T\kappa_i^\epsilon\right) + \frac{A}{2}\sum_{i=1}^{n}(\kappa_i^\epsilon)^2 \tag{2.30}$$

At this stage, the following matrices are identified to simplify the expression:

$$[A_\theta] = A \sum_{i=1}^{n} [B_{\theta i}]^T [B_{\theta i}] \tag{2.31}$$

$$\{b_\theta\} = A \sum_{i=1}^{n} [B_{\theta i}]^T \kappa_i^\epsilon \tag{2.32}$$

The bending contribution to the functional is thus expressed as:

$$\Phi_\theta = \frac{1}{2}\{q\}^T [A_\theta]\{q\} - \{q\}^T \{b_\theta\} + C \tag{2.33}$$

where $C$ represents a constant term independent of the nodal displacements. The discretized functional is minimized with respect to the nodal degrees of freedom. By taking the partial derivative of $\Phi_\theta$ with respect to the vector $\{q\}$ and setting it to zero, the following relation is obtained:

$$\frac{\partial \Phi_\theta}{\partial \{q\}} = [A_\theta]\{q\} - \{b_\theta\} = 0 \tag{2.34}$$

Consequently, the resolving system for the bending component is defined as:

$$[A_\theta]\{q\} = \{b_\theta\} \tag{2.35}$$

This linear system allows for the reconstruction of the nodal displacements based on the experimental strain data provided by the sensors.

### 2.2.3 Zigzag contribution ($\phi$)

The third term of the functional represents the contribution of the zigzag effect, which accounts for the kinematic enrichment of the Refined Zigzag Theory:

$$\Phi_\psi = \frac{A}{2} \int_0^L \left[\psi_{,x} - \mu^\epsilon\right]^2 dx \approx \frac{A}{2} \sum_{i=1}^{n} \left[\psi_{,xi} - \mu_i^\epsilon\right]^2 \tag{2.36}$$

The zigzag function $\psi$ is interpolated using the linear shape functions $L_1$ and $L_2$:

$$\psi = [0\ 0\ 0\ L_1\ 0\ 0\ 0\ L_2]\{q\} \tag{2.37}$$

The analytical zigzag strain gradient $\psi_{,x}$ is obtained as:

$$\psi_{,x} = [0\ 0\ 0\ L_{1,x}\ 0\ 0\ 0\ L_{2,x}]\{q\} = [B_\psi]\{q\} \tag{2.38}$$

For the development of the functional, the transposed form of the analytical gradient is used:

$$\psi_{,x}^{T} = \{q\}^{T}[B_{\psi}]^{T} \tag{2.39}$$

Substituting the discretization into the zigzag term of the functional leads to:

$$\Phi_{\psi} = \frac{A}{2}\sum_{i=1}^{n}\left(\psi_{,xi} - \mu_i^{\epsilon}\right)^{T}\left(\psi_{,xi} - \mu_i^{\epsilon}\right) \tag{2.40}$$

By substituting the kinematic relation into Eq. (2.39), the expression becomes:

$$\Phi_{\psi} = \frac{A}{2}\sum_{i=1}^{n}\left(\{q\}^{T}[B_{\psi i}]^{T} - \mu_i^{\epsilon}\right)\left([B_{\psi i}]\{q\} - \mu_i^{\epsilon}\right) \tag{2.41}$$

Expanding the product within the summation yields:

$$\Phi_{\psi} = \frac{A}{2}\sum_{i=1}^{n}\left(\{q\}^{T}[B_{\psi i}]^{T}[B_{\psi i}]\{q\} + (\mu_i^{\epsilon})^{2} - 2\{q\}^{T}[B_{\psi i}]^{T}\mu_i^{\epsilon}\right) \tag{2.42}$$

Through the property of linearity, the summation is split into three distinct terms:

$$\Phi_{\psi} = \frac{1}{2}\{q\}^{T}\left(A\sum_{i=1}^{n}[B_{\psi i}]^{T}[B_{\psi i}]\right)\{q\} - \{q\}^{T}\left(A\sum_{i=1}^{n}[B_{\psi i}]^{T}\mu_i^{\epsilon}\right) + \frac{A}{2}\sum_{i=1}^{n}(\mu_i^{\epsilon})^{2} \tag{2.43}$$

At this stage, the following matrices are identified to simplify the expression:

$$[A_{\psi}] = A\sum_{i=1}^{n}[B_{\psi i}]^{T}[B_{\psi i}] \tag{2.44}$$

$$\{b_{\psi}\} = A\sum_{i=1}^{n}[B_{\psi i}]^{T}\mu_i^{\epsilon} \tag{2.45}$$

The contribution of the zigzag effect to the functional is thus expressed as:

$$\Phi_{\psi} = \frac{1}{2}\{q\}^{T}[A_{\psi}]\{q\} - \{q\}^{T}\{b_{\psi}\} + C \tag{2.46}$$

where $C$ represents a constant term independent of the nodal displacements. The discretized functional is minimized with respect to the nodal degrees of freedom. By taking the partial derivative of $\Phi_{\psi}$ with respect to the vector $\{q\}$ and setting it to zero, the following relation is obtained:

$$\frac{\partial\Phi_{\psi}}{\partial\{q\}} = [A_{\psi}]\{q\} - \{b_{\psi}\} = 0 \tag{2.47}$$

Consequently, the resolving system for the zigzag component is defined as:

$$[A_{\psi}]\{q\} = \{b_{\psi}\} \tag{2.48}$$

### 2.2.4 Zigzag transverse shear ($\eta$)

The fourth term of the functional represents the transverse shear strain $\eta$, which is governed by the penalty parameter $\alpha$ and the equilibrium activation parameter $e$:

$$\begin{aligned}\Phi_\eta &= \frac{1}{2}[e+(1-e)\alpha]\int_0^L \left[(w_{,x}+\theta-\psi)-e\eta^\epsilon\right]^2 dx \\ &\approx \frac{1}{2}[e+(1-e)\alpha]\sum_{i=1}^{n}\left[(w_{,x}+\theta-\psi)_i-e\eta_i^\epsilon\right]^2\end{aligned} \tag{2.49}$$

The transverse shear strain is expressed through the kinematic relation:

$$(w_{,x}+\theta-\psi) = [B_\eta]\{q\} \tag{2.50}$$

where the matrix $[B_\eta]$ is defined by the spatial derivatives of the deflection shape functions and the shape functions of rotation and zigzag:

$$\begin{aligned}[B_\eta] = [0 \quad L_{1,x} \quad \left(L_1-\frac{L}{8}p_{m,x}\right) \quad \left(-L_1-\frac{cL}{8}p_{m,x}\right) \\ 0 \quad L_{2,x} \quad \left(L_2+\frac{L}{8}p_{m,x}\right) \quad \left(-L_2+\frac{cL}{8}p_{m,x}\right)]\end{aligned} \tag{2.51}$$

Consequently, for the development of the functional, the transposed form is obtained:

$$\eta_{,x}^T = \{q\}^T[B_\eta]^T \tag{2.52}$$

By substituting this discretization into Eq. (2.52), the expression becomes:

$$\begin{aligned}\Phi_\eta &= \frac{1}{2}[e+(1-e)\alpha]\int_0^L \left[(w_{,x}+\theta-\psi)-e\eta^\epsilon\right]^2 dx \\ &\approx \frac{1}{2}[e+(1-e)\alpha]\sum_{i=1}^{n}\left([B_{\eta i}]\{q\}-e\eta_i^\epsilon\right)^T\left([B_{\eta i}]\{q\}-e\eta_i^\epsilon\right)\end{aligned} \tag{2.53}$$

Expanding the product within the summation:

$$\Phi_\eta = \frac{1}{2}[e+(1-e)\alpha]\sum_{i=1}^{n}\left(\{q\}^T[B_{\eta i}]^T[B_{\eta i}]\{q\}+(e\eta_i^\epsilon)^2-2\{q\}^T[B_{\eta i}]^T e\eta_i^\epsilon\right) \tag{2.54}$$

Through the property of linearity, the expression is reorganized as:

$$\begin{aligned}\Phi_\eta =& \frac{1}{2}\{q\}^T\left([e+(1-e)\alpha]\sum_{i=1}^{n}[B_{\eta i}]^T[B_{\eta i}]\right)\{q\} \\ &-\{q\}^T\left([e+(1-e)\alpha]\sum_{i=1}^{n}[B_{\eta i}]^T e\eta_i^\epsilon\right)+C\end{aligned} \tag{2.55}$$

At this stage, the following matrices are identified to simplify the expression:

$$[A_\eta] = [e + (1-e)\alpha] \sum_{i=1}^{n} [B_{\eta i}]^T [B_{\eta i}] \tag{2.56}$$

$$\{b_\eta\} = [e + (1-e)\alpha] \sum_{i=1}^{n} [B_{\eta i}]^T e\eta_i^\epsilon \tag{2.57}$$

The contribution of the transverse shear to the functional is thus expressed as:

$$\Phi_\eta = \frac{1}{2}\{q\}^T [A_\eta]\{q\} - \{q\}^T \{b_\eta\} + C \tag{2.58}$$

where $C$ is a constant term independent of the nodal displacements. The functional is minimized with respect to the nodal degrees of freedom. By taking the partial derivative of $\Phi_\eta$ with respect to the vector $\{q\}$ and setting it to zero, the resolving system is obtained:

$$\frac{\partial \Phi_\eta}{\partial \{q\}} = [A_\eta]\{q\} - \{b_\eta\} = 0 \implies [A_\eta]\{q\} = \{b_\eta\} \tag{2.59}$$

### 2.2.5 Average transverse shear strain($\gamma$)

The fifth and final term of the functional represents the global transverse shear strain $\gamma$. This term accounts for the classic Timoshenko-like shear contribution and is governed exclusively by the equilibrium activation parameter $e$:

$$\begin{aligned} \Phi_\gamma = & \frac{1}{2} e \int_0^L \left[(w_{,x} + \theta) - \gamma^\epsilon\right]^2 dx \approx \\ & \frac{1}{2} e \sum_{i=1}^{n} \left[(w_{,x} + \theta)_i - \gamma_i^\epsilon\right]^T \cdot \left[(w_{,x} + \theta)_i - \gamma_i^\epsilon\right] \end{aligned} \tag{2.60}$$

The kinematic relation for the global shear strain is defined as

$$(w_{,x} + \theta) = [B_\gamma]\{q\} \tag{2.61}$$

where the matrix $[B_\gamma]$ is defined by incorporating the spatial derivatives of the deflection shape functions and the rotation shape functions as follows:

$$[B_\gamma] = \begin{bmatrix} 0 & L_{1,x} & \left(L_1 - \frac{L}{8} p_{m,x}\right) & \left(-\frac{cL}{8} p_{m,x}\right) \\ 0 & L_{2,x} & \left(L_2 + \frac{L}{8} p_{m,x}\right) & \left(\frac{cL}{8} p_{m,x}\right) \end{bmatrix} \tag{2.62}$$

Consequently, for the development of the functional, the transposed form is obtained:

$$\gamma_{,x}^{T} = \{q\}^{T}[B_{\gamma}]^{T} \tag{2.63}$$

By substituting the kinematic relation into Eq. (2.63) and expanding the quadratic expression, the functional becomes:

$$\Phi_{\gamma} = \frac{1}{2} e \sum_{i=1}^{n} \left( \{q\}^{T}[B_{\gamma i}]^{T}[B_{\gamma i}]\{q\} + (\gamma_{i}^{\epsilon})^{2} - 2\{q\}^{T}[B_{\gamma i}]^{T}\gamma_{i}^{\epsilon} \right) \tag{2.64}$$

[1] Applying the property of linearity and factoring in the vector $\{q\}$, the following matrices are identified:

$$[A_{\gamma}] = e \sum_{i=1}^{n} [B_{\gamma i}]^{T}[B_{\gamma i}] \tag{2.65}$$

$$\{b_{\gamma}\} = e \sum_{i=1}^{n} [B_{\gamma i}]^{T} e \gamma_{i}^{\epsilon} \tag{2.66}$$

The global shear contribution to the functional is thus simplified as:

$$\Phi_{\gamma} = \frac{1}{2}\{q\}^{T}[A_{\gamma}]\{q\} - \{q\}^{T}\{b_{\gamma}\} + C \tag{2.67}$$

where $C$ is a constant independent of the nodal variables. To find the stationary point, the partial derivative with respect to $\{q\}$ is set to zero, resulting in the following resolving system for this component:

$$\frac{\partial \Phi_{\gamma}}{\partial \{q\}} = [A_{\gamma}]\{q\} - \{b_{\gamma}\} = 0 \implies [A_{\gamma}]\{q\} = \{b_{\gamma}\} \tag{2.68}$$

### 2.2.6 Element assembly

The final resolving system for the inverse finite element is obtained by summing the contributions from all five strain components. The global stationarity of the functional leads to the following linear algebraic system:

$$[A]\{q\} = \{b\} \tag{2.69}$$

[1] The index $i$ in the various summations refers to the specific locations where the sensors are positioned. It is important to note that the sets of measurement points $i$ for the membrane, bending, and zigzag terms $(u, \theta, \psi)$ do not necessarily coincide with those used for the transverse and global shear terms $(\eta, \gamma)$, which may instead refer to numerical integration points.

where the global inverse stiffness matrix $[A]$ is the sum of the individual contributions:

$$[A] = [A_u] + [A_\theta] + [A_\psi] + [A_\eta] + [A_\gamma] \tag{2.70}$$

and the global sensor data vector $\{b\}$ is:

$$\{b\} = \{b_u\} + \{b_\theta\} + \{b_\psi\} + \{b_\eta\} + \{b_\gamma\} \tag{2.71}$$

Recalling the individual definitions, the global matrix can be expressed to highlight the role of the equilibrium parameter $e$ and the penalty factor $\alpha$:

$$[A] = [A_u] + [A_\theta] + [A_\psi] + (e + (1 - e)\alpha)[A_\eta] + e[A_\gamma] \tag{2.72}$$

In this context, the matrix $[A]$ is purely geometric and depends only on the sensor locations and the element length, allowing it to be computed and inverted only once. The vector $\{b\}$, instead, is updated in real-time as new strain measurements are acquired from the sensors, enabling the instantaneous reconstruction of the entire displacement field $\{q\}$.

# Chapter 3

# Numerical implementation in MATLAB

This chapter illustrates the numerical conversion of the theoretical formulation set out in Chapter 2. The main aim is to create a computer algorithm in a *MATLAB* environment, capable of tackling the inverse sandwich beam problem through the *iFEM* approach.
The code is designed to handle data derived from a direct model, which is used to emulate experimental sensor readings, and to solve the resulting assembled linear system. This procedure allows to completely reconstruct of the state of deformation of the entire structure,

## 3.1 Algorithm structure and global assembly

The core of the code is based on a main loop that iterates through the finite elements ($n_e$) into which the beam is divided. To maintain the integrity of the entire system, the algorithm uses three essential data structure:

- **Global nodal coordinate matrix** ($p_n$): indicates the $(x, z)$ coordinates of each node.
- **Connectivity matrix** ($C_{ne}$): specifies which nodes belong to each element.
- **Grade of Freedom Matrix (DoF)** ($C_{se}$): associates the local degrees of freedom of each element with their positions in the overall system. [8]

Assembly occurs cumulatively: for each element,v the algorithm determines the local matrix [$A\_e$] and the local vector $b\_e$. These contributions are added to the designated positions of the global matrix. This methodology, implemented

in *MATLAB* through specific operations: `A(I,I) = A(I,I) + A_e` and `b(I,1) = b(I,1) + b_e`, ensures that the contributions from adjacent elements sharing the same nodes are correctly summed, thus allowing the creation of the entire system.

### 3.1.1 Input data processing and kinematic variable estimation

Processing the strain data provided by the direct model is the initial step of the procedure, which simulates experimental measurements. A matrix is used to collect these data, which includes axial strain values $\epsilon_x$ collected at specific longitudinal ($x$) and transverse ($z$) coordinates. According to the **Refined Zig-Zag Theory (RZT)**, the axial strain at every point within the cross-section is specified as:

$$\epsilon_x = u_{,x} + z\theta_{,x} + \phi^k(z)\psi_{,x} \tag{3.1}$$

where:

- $u_{,x}$: membrane strain ($\epsilon$).
- $\theta_{,x}$: bending curvature ($\kappa$).
- $\phi_{,x}$: zigzag strain ($\mu$).

Three strain values are obtained for every measuring station $i$ along the beam axis at three different heights: $z_1$, $z_2$ and $z_3$. By using this, it is possible to create a system of three linear equations with unknowns such as $\epsilon_{,x}$, $\kappa_{,x}$ and $\mu_{,x}$:

$$\begin{cases} \epsilon_{xi}^{(1)} = \epsilon_i + z_1\kappa_i + \phi(z_1)\mu_i \\ \epsilon_{xi}^{(2)} = \epsilon_i + z_2\kappa_i + \phi(z_2)\mu_i \\ \epsilon_{xi}^{(3)} = \epsilon_i + z_3\kappa_i + \phi(z_3)\mu_i \end{cases} \tag{3.2}$$

In order to set up and compute the system (3.2), the measurement matrix $[M]$ must first be constructed. This matrix is organized into three columns containing, respectively, the longitudinal coordinates of the sensors ($x$), the transverse coordinates ($z$) and the strain values ($\epsilon$), all previously extracted from the direct model. The $[M]$ matrix allows the problem to be managed and solved on an element-by-element basis, indeed each block of rows containing the $x$, $z$ and $\epsilon$ triplets uniquely corresponds to a specific measurement station assigned to a single inverse element. The `backslash operator` is used in *MATLAB* to uniquely determine the kinematic variables for each station in this system. It is important to note that this calculation is required before any further action; the calculated data ($\epsilon_{,x}$, $\kappa_{,x}$ and $\mu_{,x}$) serve as experimental targets for vectors $\{b_u\}, \{b_\theta\}, \{b_\phi\}$ and define the matrices $[A_u], [A_\theta], [A_\phi]$. Regardless of whether the equilibrium parameter is deactivated ($e = 0$) or activated ($e = 1$) this process remains the same.

### 3.1.2 Equilibrium targets formulation for the $e = 1$ case

Setting the equilibrium activation parameter to $e = 1$ allows to *iFEM functional* to transcend only the kinamtic data provided by the sensors. In this configuration, the contribution of the average transverse shear ($\gamma^\epsilon$ and transverse shear ($\eta^\epsilon$) are also included. Since these components are not directly detectable on the surface, their determination occurs analytically by enforcing compliance with the cross-sectional equilibrium equantions, ensuring the physical consistency ogf the model.
As established in the theoretical framework presented in the previous chapter 1, the connection between stress resultants and the variables $\epsilon$, $\kappa$ and $\mu$ is exploited to determine the shear state. By sustituting the constitutive relations into the indefinite equations, the unknown $\gamma^\epsilon$ and $\gamma^\epsilon$ can be expressed solely as a functional of the spatial derivatives of the strain, namely $\epsilon_{,x}$, $\kappa_{,x}$ and $\mu_{,x}$.
To accurately define the equilibrium targets, the model must first determine the spatial derivatives of the strains ($\epsilon_{,x}$, $\kappa_{,x}$ and $\mu_{,x}$). Rather than calculating these derivatives locally on an element-by-element basis a global reconstruction over the entire structure was adopted. This choice ensures a much cleaner comparison between the direct and inverse models.
In practice, the algorithm interpolates the sensor data across the whole beam using a single parabolic profile for each variable ($\epsilon$, $\kappa$ and $\mu$). Fitting these second-degree polynomials provides a smooth, continuous representation of the strains along the axis. Consequently, their spatial derivatives naturally follow a consistent linear trend from one end of the beam to the other.
This entire calculation takes place during a pre-processing phase, just before the main assembly loop. Assuming the structure is discretized into three elements, the algorithm places two points within each element (at 20% and 80% of their local length). At each of these of these six station, tracked in the code by their absolute x-coordinates, the following sequence occurs:

- **Evolution of strain derivatives**: the spatial derivatives of the kinematic variables ($\epsilon_{,x}$, $\kappa_{,x}$ and $\mu_{,x}$) are extracted analytically directly from the polynomial coefficients.
- **Solving the shear system**: these gradients are then fed into a $2 \times 2$ linear system
- **Target determination**: solving this system directly outputs the global shear ($\gamma^\epsilon$) and transverse shear ($\eta^\epsilon$) strains required to complete the iFEM functional.

## 3.2 Data generation and validation through the Direct Model

To validate the inverse algorithm, the numerical test campaign utilized a structural FEM code based on a direct approach. This computational environment models the statics of the sandwich beam by strictly implementing the kinematics of the Refined Zig-Zag Theory (RZT). After defining the modular architecture of the laminate, along with the load and boundary conditions, the global system is solved to compute the displacement and strain fields. It is important to note that these fields are not exact analytical solutions, but rather numerical approximations obtained through a direct FEM model that employs the same shape functions and degrees of freedom (DOFs) as the inverse elements to be verified.
From this direct simulation, two fundamental datasets were extracted to feed the inverse problem:

1. The axial strains $\epsilon_x$ were sampled in discrete coordinates, which are used to simulate the readings of the virtual sensor network.

2. The numerical values of the average transverse shear strain measure ($\gamma$) and the zigzag transverse shear strain measure ($\eta$) evaluated within each element.

In the initial validation phase of the iFEM algorithm, these reference shear values were explicitly inserted into the load vector. This step isolated the solver's response, allowing the verification of the correct formulation of the iFEM stiffness matrices and their global assembly. Only after confirming the perfect convergence of the inverse model under these ideal conditions were the exact parameters removed to test the code's true predictive capability using shear targets autonomously derived from the equilibrium equations.

### 3.2.1 Analysis of results using direct shear data - Validation phase

Before proceeding with the numerical validation of the inverse model, it is necessary to define the physical and mechanical characteristics of the analyzed structure. The test case consists of a sandwich beam with a total length of $L = 300mm$; the laminate features a three-layer architecture: two outer sheets made of Ergal and an inner core made of foam.
Regarding the loading conditions, the beam is subjected to a concentrated downward load applied at the free end of the right. A schematic representation of the geometry, materials, load configuration and degree of freedom is illustrated in Figure 3.1
Once the physical model was defined, the $300mm$ domain was discretized using a uniform mesh consisting of 3 inverse elements, corresponding to a total of 4

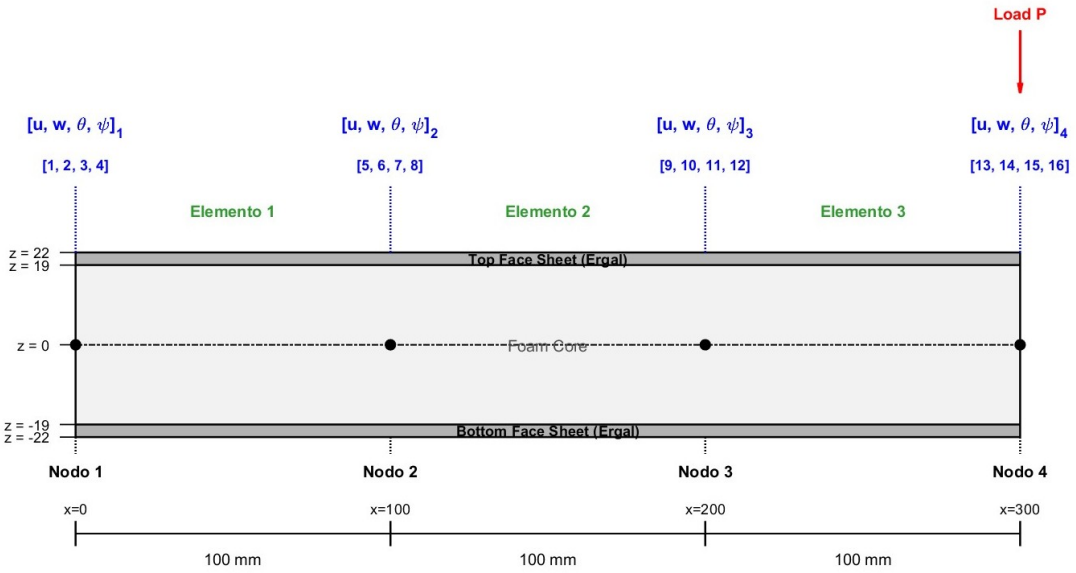


**Figure 3.1:** Cross-section and z-coordinate reference system

structural nodes spaced $100mm$ apart.
To properly feed the *iFEM* algorithm, the specific measurement matrix $[M]$ was constructed. Consistently with the adopted mesh, the virtual strain sensors were positioned in $x = 50mm$, $x = 150mm$ and $x = 250mm$. For each station, three strain values were extracted at specific transverse coordinates ($z = -22mm$, $z = -19mm$ and $z = 22$) which depend on the layer of the sandwich. Resulting in the following $9 \times 3$ input matrix:

$$[M] = \begin{bmatrix} 50 & -22 & 3.5205 \times 10^{-4} \\ 50 & -19 & -2.9167 \times 10^{-5} \\ 50 & 22 & -3.5205 \times 10^{-4} \\ 150 & -22 & 8.1938 \times 10^{-5} \\ 150 & -19 & 1.1791 \times 10^{-4} \\ 150 & 22 & -8.1938 \times 10^{-5} \\ 250 & -22 & 3.9499 \times 10^{-5} \\ 250 & -19 & 2.6542 \times 10^{-5} \\ 250 & 22 & -3.9499 \times 10^{-5} \end{bmatrix}$$

The boundary conditions imposed on the system to solve the linear problem are defined by the constraint vector `ib = [1, 3, 4, 14]`. From a physical perspective, this condition required constraining the following degrees of freedom:

- At **Node 1** ($x = 0[mm]$), the axial displacement, bending rotation, and zigzag amplitude are constrained ($u_1 = \theta_1 = \phi_1 = 0$).

- At **Node 4** ($x = 300[mm]$), the transverse displacement is constrained.

Tables 3.1 and 3.2 summarize the nodal responses obtained by feeding the iFEM functional with direct shear data ($\gamma$ and $\eta$) extracted from the direct model. As can be seen from the values, using these exact target inputs produces outstanding agreement between the inverse reconstruction and the direct reference model for both formulations.

| **Node** | **DOF** | **Direct** $c = -1$ | **iFEM (e = 0)** | **Error %** |
|---|---|---|---|---|
| **Node 1** (0 mm) | $u_1$ [1] | 0.0000e+00 | 0.0000e+00 | 0.00 % |
| | $w_1$ [2] | -3.0207e+00 | -3.0200e+00 | 0.02 % |
| | $\theta_1$ [3] | 0.0000e+00 | 0.0000e+00 | 0.00 % |
| | $\phi_1$ [4] | 0.0000e+00 | 0.0000e+00 | 0.00 % |
| **Node 2** (100 mm) | $u_2$ [5] | 0.0000e+00 | 0.0000e+00 | 0.00 % |
| | $w_2$ [6] | -2.3836e+00 | -2.3843e+00 | 0.03 % |
| | $\theta_2$ [7] | -1.6002e-03 | -1.6002e-03 | 0.00 % |
| | $\phi_2$ [8] | 1.1130e-02 | 1.1113e-02 | 0.15 % |
| **Node 3** (200 mm) | $u_3$ [9] | 0.0000e+00 | 0.0000e+00 | 0.00 % |
| | $w_3$ [10] | -1.1727e+00 | -1.1729e+00 | 0.02 % |
| | $\theta_3$ [11] | -1.9727e-03 | -1.9727e-03 | 0.00 % |
| | $\phi_3$ [12] | 9.5408e-03 | 9.5408e-03 | 0.00 % |
| **Node 4** (300 mm) | $u_4$ [13] | 0.0000e+00 | 0.0000e+00 | 0.00 % |
| | $w_4$ [14] | 0.0000e+00 | 0.0000e+00 | 0.00 % |
| | $\theta_4$ [15] | -2.1522e-03 | -2.1522e-03 | 0.00 % |
| | $\phi_4$ [16] | 9.7933e-03 | 9.7933e-03 | 0.00 % |

**Table 3.1:** Nodal displacements e = 0

| **Node** | **DOF** | **Direct** $c = B_{44L}/A_{44L}$ | **iFEM (e = 1)** | **Error %** |
|---|---|---|---|---|
| **Node 1** (0 mm) | $u_1$ [1] | 0.0000e+00 | 0.0000e+00 | 0.00 % |
| | $w_1$ [2] | -3.0207e+00 | -3.0208e+00 | 0.00 % |
| | $\theta_1$ [3] | 0.0000e+00 | 0.0000e+00 | 0.00 % |
| | $\phi_1$ [4] | 0.0000e+00 | 0.0000e+00 | 0.00 % |
| **Node 2** (100 mm) | $u_2$ [5] | 0.0000e+00 | 0.0000e+00 | 0.00 % |
| | $w_2$ [6] | -2.3836e+00 | -2.3837e+00 | 0.00 % |
| | $\theta_2$ [7] | -1.6002e-03 | -1.6002e-03 | 0.00 % |
| | $\phi_2$ [8] | 1.1130e-02 | 1.1118e-02 | 0.11 % |
| **Node 3** (200 mm) | $u_3$ [9] | 0.0000e+00 | 0.0000e+00 | 0.00 % |
| | $w_3$ [10] | -1.1727e+00 | -1.1727e+00 | 0.00 % |
| | $\theta_3$ [11] | -1.9727e-03 | -1.9727e-03 | 0.00 % |
| | $\phi_3$ [12] | 9.5408e-03 | 9.5383e-03 | 0.03 % |
| **Node 4** (300 mm) | $u_4$ [13] | 0.0000e+00 | 0.0000e+00 | 0.00 % |
| | $w_4$ [14] | 0.0000e+00 | 0.0000e+00 | 0.00 % |
| | $\theta_4$ [15] | -2.1522e-03 | -2.1522e-03 | 0.00 % |
| | $\phi_4$ [16] | 9.7933e-03 | 9.7930e-03 | 0.00 % |

**Table 3.2:** Nodal displacements comparison using direct shear input (e = 1)

This minimal numerical discrepancy (with maximum relative errors generally below 0.05% rigorously certifies the correct implementation of the iFEM stiffness matrices and their assembly into the global system, thereby validating the algorithm's architecture prior to the introduction of the cross-sectional equilibrium equations. Furthermore, feeding the exact shear data highlights an almost total convergence between the $e = 0$ and $e = 1$. The numerical discrepancy between the two configurations is practically negligible, being on the order of $10^{-4}$ mm for the transverse displacement $w$, confirming that both formulations are inherently consistent when supplied with ideal physical inputs.

## 3.3 Data generation and validation through the Equilibrium Equations

Once the iFEM algorithm was validated against the direct model, the equilibrium equations were explicitly activated. In this new operational scenario, characterized by the absence of direct measurements regarding the transverse shear strain, the necessary shear parameters (the global transverse shear strain $\gamma$ and the zigzag amplitude $\eta$) are no longer imported from the outside. Instead, they are derived entirely autonomously by solving the cross-sectional equilibrium equations. In particular, the algorithm employes the spatial derivatives of the kinamtic variable

$(\epsilon_{,x}, \kappa_{,x}, \mu_{,x})$, which have been previously estimated by polynomial interpolation of the sensor data, to find the solution of the linear system that is influenced by the stiffness of beam. $(A_{44}, B_{44}, etc)$. The numerical values derived from this analytical procedure are evaluated at the local coordinates ($0.2L$ and $0.8L$) within each finite element. In this way, the iFEM functional becomes self-sufficient: it leverages the physical and mechanical consistency of the sandwich beam to compensate for the lack of shear sensors, constraining the reconstruction of the transverse displacement field $w$ to satisfy the internal load equilibrium. To evaluate the effectiveness of this autonomous estimation, the analysis was performed while keeping the initial structural configuration strictly unchanged. Specifically, the total length of the beam ($L = 300[mm]$), the spatial discrertization (3 imverse finite elements), and the constrained degrees of freedom ($u_1 = \theta_1 = \phi_1 = 0$ at Node 1 and $w_4 = 0$ at Node 4) remained identical to those used in the validation phase.
Tables 3.3 and 3.4 reports the new nodal displacement field. In this case, the results in the column ($e = 1$) are obtained by feeding the iFEM functional exclusively with the shear targets ($\gamma$ and $\eta$) analytically calculated through the cross-sectional equilibrium equations.

| **Node** | **DOF** | **Direct** $c = -1$ | **iFEM (e = 0)** | **Error %** |
|---|---|---|---|---|
| **Node 1** (0 mm) | $u_1$ [1] | 0.0000e+00 | 0.0000e+00 | 0.00 % |
| | $w_1$ [2] | -3.0207e+00 | -3.0200e+00 | 0.02 % |
| | $\theta_1$ [3] | 0.0000e+00 | 0.0000e+00 | 0.00 % |
| | $\phi_1$ [4] | 0.0000e+00 | 0.0000e+00 | 0.00 % |
| **Node 2** (100 mm) | $u_2$ [5] | 0.0000e+00 | 0.0000e+00 | 0.00 % |
| | $w_2$ [6] | -2.3836e+00 | -2.3843e+00 | 0.03 % |
| | $\theta_2$ [7] | -1.6002e-03 | -1.6002e-03 | 0.00 % |
| | $\phi_2$ [8] | 1.1130e-02 | 1.1113e-02 | 0.15 % |
| **Node 3** (200 mm) | $u_3$ [9] | 0.0000e+00 | 0.0000e+00 | 0.00 % |
| | $w_3$ [10] | -1.1727e+00 | -1.1729e+00 | 0.02 % |
| | $\theta_3$ [11] | -1.9727e-03 | -1.9727e-03 | 0.00 % |
| | $\phi_3$ [12] | 9.5408e-03 | 9.5408e-03 | 0.00 % |
| **Node 4** (300 mm) | $u_4$ [13] | 0.0000e+00 | 0.0000e+00 | 0.00 % |
| | $w_4$ [14] | 0.0000e+00 | 0.0000e+00 | 0.00 % |
| | $\theta_4$ [15] | -2.1522e-03 | -2.1522e-03 | 0.00 % |
| | $\phi_4$ [16] | 9.7933e-03 | 9.7933e-03 | 0.00 % |

**Table 3.3:** Nodal displacements e = 0

| **Node** | **DOF** | **Direct** $c = B_{44L}/A_{44L}$ | **iFEM (e = 1)** | **Error %** |
|---|---|---|---|---|
| **Node 1** (0 mm) | $u_1$ [1] | 0.0000e+00 | 0.0000e+00 | 0.00 % |
| | $w_1$ [2] | -3.0207e+00 | -3.1036e+00 | 2.74 % |
| | $\theta_1$ [3] | 0.0000e+00 | 0.0000e+00 | 0.00 % |
| | $\phi_1$ [4] | 0.0000e+00 | 0.0000e+00 | 0.00 % |
| **Node 2** (100 mm) | $u_2$ [5] | 0.0000e+00 | 0.0000e+00 | 0.00 % |
| | $w_2$ [6] | -2.3836e+00 | -2.3782e+00 | 0.23 % |
| | $\theta_2$ [7] | -1.6002e-03 | -1.6002e-03 | 0.00 % |
| | $\phi_2$ [8] | 1.1130e-02 | 1.0061e-02 | 9.60 % |
| **Node 3** (200 mm) | $u_3$ [9] | 0.0000e+00 | 0.0000e+00 | 0.00 % |
| | $w_3$ [10] | -1.1727e+00 | -1.2295e+00 | 4.84 % |
| | $\theta_3$ [11] | -1.9727e-03 | -1.9727e-03 | 0.00 % |
| | $\phi_3$ [12] | 9.5408e-03 | 9.7082e-03 | 1.75 % |
| **Node 4** (300 mm) | $u_4$ [13] | 0.0000e+00 | 0.0000e+00 | 0.00 % |
| | $w_4$ [14] | 0.0000e+00 | 0.0000e+00 | 0.00 % |
| | $\theta_4$ [15] | -2.1522e-03 | -2.1522e-03 | 0.00 % |
| | $\phi_4$ [16] | 9.7933e-03 | 1.0722e-02 | 9.48 % |

**Table 3.4:** Nodal displacements comparison using equilibrium equations (e = 1)

Unlike the validation phase, comparing the $e = 0$ with $e = 1$ now reveals a clear and physically meaningful difference in the displacement field.
Particularly for the transverse displacement $w$, the magnitude increases when the shear parameters are activated (for instance, at Node 1, $w_1$ goes from -3.0200e+00 mm to -3.1036e+00). This variation highligths the capability of the algorithm to capture the additional flexibility introduced by the shear deformability, which is characteristic of sandwich structures. Having successfully verified this capability, it is important to specify that for all subsequent inverse analyses presented in this work, the $e = 1$ formulation will exclusively operate by recovering the shear strain ($\gamma$ and $\eta$) through the analytical solution of the cross-sectional equilibrium equations, ensuring a completely autonomous reconstruction process.

# Chapter 4

# Numerical assessment

This chapter discusses the comparison between the numerical implementation of the *iFEM* model developed in the *MATLAB* setting and the outcomes derived from a sophisticated finite element model *FEM* produced with *MSC Patran/Nastran* software. The latter provides a reference numerical solution that aims to replicate the real structural behavior of the sandwich beam.
The comparison focuses on the ability of the *iFEM* algorithm to converge toward the reference results, analyzing both the effectiveness of the sensor-based reconstruction and the impact of integrating the equilibrium equations for the autonomous estimation of transverse shear strains.

## 4.1 The simulation environment: MSC Patran

For the development of the numerical model and the analysis results, MSC Patran was employed. It is an advanced software environment dedicated exclusively to pre- and post-processing for Finute Elementi Analysis (FEA). Unlike traditional CAD systems, Patran is specifically designed to translate continuous geometry into a discrete domain, providing algorithms for topological cleanup and the generation of both structured and unstructured meshes. The software acts as a management interface for various solver allowing for the visual definition of loads, boundary conditions, and material properties without the need to directly manipulate the input code. Falling within the framework of Virtual Product Development (VPD), Patran enables the centralization of the entire virtual structural validation process within a single platform. [9]

### 4.1.1 Model automation via Session file

To ensure the highest level of accuracy and reproducibility in numerical validation, the construction of the finite element model within the MSC Patran environment was fully automated. For this purpose a dedicated Session File (*.ses*) based on the **Patran Command Language (PCL)** was developed. PCL is the advanced, native programming language of Patran, utilized to write macros, develop custom functions, and parametrically drive the software.
Essentially a session file is a text script that compiles a logical sequence of PCL instructions. Executing this file allows batch processing of modeling commands, eliminating the need for manual, repetitive, and error-prone interactions with the Graphical User Interface [10] .
In this thesis, the **PCL** code is structured to define all the fundamental aspects of the simulation:

- **Geometry and discretization (meshing)**: the script generates the physical dimensions of the sandwich beam and performs the numerical discretization.
- **Boundary conditions and loads**: the session file defines the kinematic constraints required to faithfully replicate the experimental setup.
- **Analysis setup**: the final part of the session file includes the parameters defining the linear static analysis ($SOL101$), automatically preparing the input required by the *MSC Nastran* to calculate the structural response of the beam.

Ultimately, this PCL-based approach allowed for instantaneous regeneration of the model when varying key parameters, such as mesh density or applied loads.

## 4.2 Geometry, material properties and test setup

The study was conducted by analyzing two specific configurations of sandwich beams, hereafter referred to **B1** and **B2**. Both share the same material composition, but differ in their geometric dimensions, such as length and total thickness. In the reference experimental setup, the beams are subjected to a standard 3-point bending test, where the distance between the lower support constraints is defined as the effective span length, $L_{eff}$. [11]
It is importante to note that the modeling strategy involved exploiting the symmetry of the system; consequently, because of the geometry of beam, the material properties and loading are symmetric relative to midspan, the finite element model developed in *MSC Patran* represen exclusively **half of the beam**. This choice was made to reduce the computational cost and optimize the mesh, provided that appropriate symmetry boundary conditions are applied to the symmetry plane.

The sandwich structure consists of the external face sheets made of a high-strength aluminum alloy (**EN-AW 7075 T6**) and an inner core made of polymeric foam (**Rohacell ® IG-31**). The experimental mechanical properties, specifically the Young's modulus ($E$) and the shear modulus ($G$), are summarized in Table 4.1 and were provided as fundamental inputs to the software. [11]

| **Material** | $E$ **[MPa]** | $G$ **[MPa]** |
|---|---|---|
| Face sheets: EN-AW 7075 T6 (Ergal) | 67545 | 25393 |
| Core: Rohacell ® IG-31 | 43.2 | 12.1 |

**Table 4.1:** Experimental mechanical properties of the sandwich beam constituens. [11]

The overall geometric dimensions of the two investigated specimens are reported in table 4.2. It should be noted that the values listed in the table ($L$, $L_{eff}$) refer to the geometry of the *entire* beam, although the PCL script was programmed to generate and discretize only its half-length ($L/2$). [11]

| **Specimen ID** | $L$ **[mm]** | $L_{eff}$ **[mm]** | $b$ **[mm]** | $h$ **[mm]** | $h_f$ **[mm]** |
|---|---|---|---|---|---|
| **B1** | 640 | 600 | 90 | 44.60 | 3 |
| **B2** | 490 | 450 | 90 | 43.30 | 3 |

**Table 4.2:** Geometric dimensions of the B1 and B2 sandwich beam specimens. [11]

To provide a clear visualization of the experimental setup and the geometric parameters discussed above, Figure 4.1 illustrates the schematic of the three-point bending test. The diagram 4.1 highlights the total length of the specimen ($L$) and the effective span between the lower support ($L_{eff}$). The cross-section geometry is further defined by the total height of the beam ($h$), the specific thickness of the external face sheets ($h_f$) and the transverse width of the section ($b$). As depicted in the schematic, the structural configuration results in a constant overhang of 20 mm at both extremities of the beam. A concentrated load, denoted as $F$, is applied precisely at the midspan. Furthermore, the global reference system is established with x-axis aligned along the longitudinal mid-plane of the sandwich core.
This exact geometric configuration and coordinate system were faithfully replicated within the *Patran* simulation environment. [11]

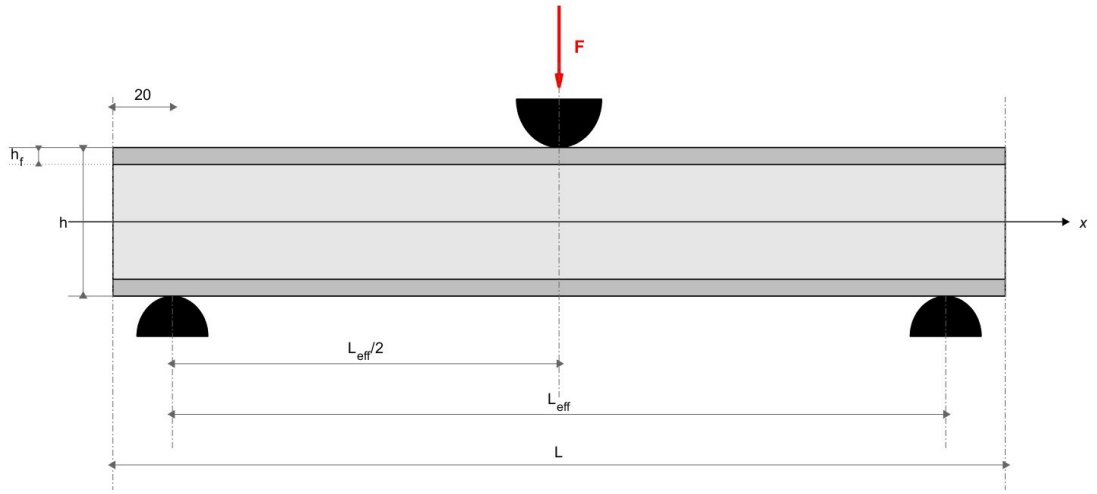


**Figure 4.1:** Schematic representation of the three-point bending test on the sandwich beam specimen.

## 4.3 Finite element discretization and boundary conditions

To accurately capture the structural response of the sandwich beam while optimizing computational resources, the longitudinal cross-section of the half-model was discretized using **2D membrane elements**. Within the MSC Patran environment, three distinct 2D property sets were defined and assigned to their respective geometric regions: the upper face sheet, the foam core and the lower face sheet. This approach allows for the correct assignment of distinct material properties (Ergal and Rohacell) and the definition of the out-of-plane thinckness, which corresponds to the constant width of the beam ($b = 90[mm]$). [11]
The boundary conditions and external loads were implemented as follows:

- **Symmetry condition**: in the middle section of the beam a symmetry condition was imposed. The nodes lying in this plane were constrained to prevent longitudinal translation (along the x-axis) to simulate the continuity of the full physical beam.
- **Support condition**: this support was positioned $20mm$ from the left free edge, perfectly replicating the actual structural overhang.
- **Load Application**: The external force was applied as a concentrated load at the top-right vertex of the model. Because the finite element model exclusively represents half of the physical specimen, the magnitude of the concentrated

load was halved compared to the total experimental value, thus ensuring a symmetric and consistent force distribution.

To faithfully simulate the physical 3-point bending test on the half-symmetry model, specific kinematic constraints and loads were applied to the finite element mesh. Figure 4.2 shows the boundary condition set up for the **B1** beam configuration; however, it should be noted that the identical simulation architecture was also adopted for the **B2** beam, consistently updating only the relevant geometric dimensions.


**Figure 4.2:** Finite element of the B1

## 4.4 Numerical solution and data extraction

After completing the finite element model, the input was generated and sent to the solver. The structural response was determined through a *linear static simulation* **SOL101**; this approach is justified by the mechanical properties of the materials and the loading conditions, both of which operate within their elastic limits under the assumption of **small displacements and deformations**.
Using the spatial coordinates provided by the report, it was possible to map and isolate the strains exclusively at the nodes located on the top and bottom face sheets, as well as at their respective interfaces with the foam. From this file, the longitudinal strain component, namely $\epsilon_{xx}$, was specifically extracted, which is the fundamental input to feed the *iFEM* algorithm developed in *MATLAB*. This procedure was carried out identically for both analyzed configurations, generating the datasets required for the model validation of the **B1** and **B2** beams.

## 4.5 Numerical results: Patran vs iFEM

This section presents and discusses the numerical results obtained from the implementation of the *iFEM* algorithm for the two investigated sandwich beam configurations, **B1** and **B2**.

### 4.5.1 Sandwich beam B1 - three sensors

As an initial reference, the **static analysis** in *MSC Patran* performed by applying a force of approximately $-422.29N$ (which corresponds to the load reached during the experimental phase), provided the exact displacement field. As shown in the contour plot of Figure 4.3, the color bands of the displacement in the y-direction (which represents the transverse deflection $w$ in the beam's local reference system) are not perfectly vertical, demonstrating that this transverse deflection varies slightly along the thickness of the cross-section. This phenomenon is strictly related to the high-fidelity nature of the $2D$ solid finite element model, where local deformations and localized indentations, caused by the punctual nature of the boundary conditions and the applied load, heavily influence the kinematic response.

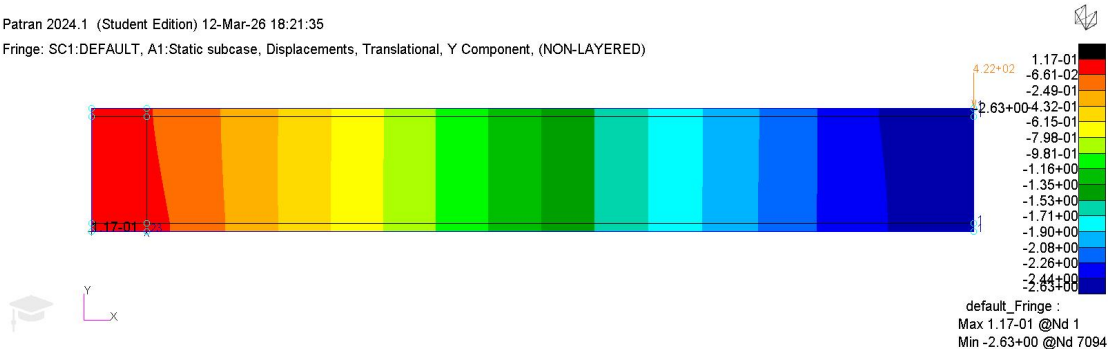


**Figure 4.3:** Displacement y-component

Conversely, the *Refined Zigzag Theory (RZT)* employed by the *iFEM* framework assumes a kinematically uniform transverse displacement $w(x)$ for any given cross-section. Therefore, to obtain a single, comparable scalar value from the Patran results, the nodal $y-$displacements were averaged along the thickness specifically at the last strip of nodes, corresponding to the section where the concentrated load is applied. Through this averaging procedure, the equivalent maximum transverse deflection resulted in approximately $-2.58mm$ (a value slightly lower than the absolute local peak of $-2.63mm$ visible in the Patran legend).

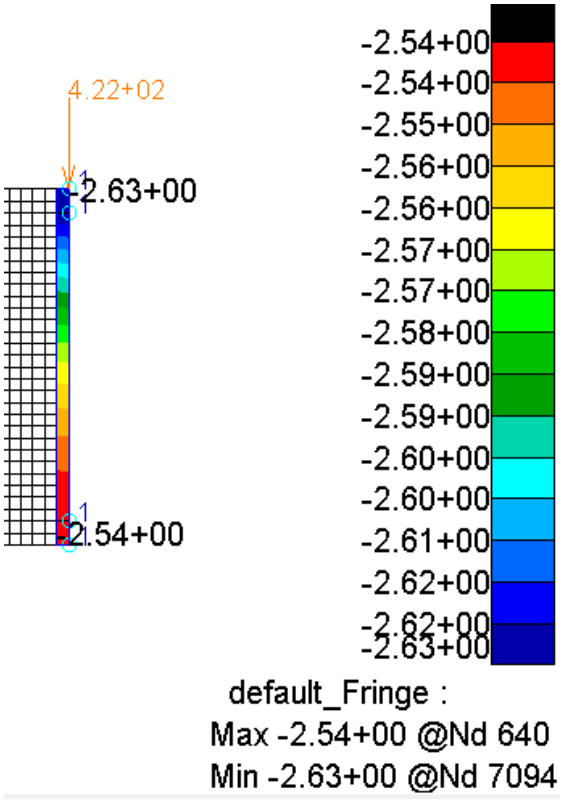


**Figure 4.4:** Detail of the transverse displacement (y-component) in the elements at the loaded section.

Subsequently, to construct the measurement matrix $[M]$, the values of the longitudinal strains ($\epsilon_{xx}$) were directly extracted from an output file exported from Patran following the static analysis. Specifically, by reading the data from this file, the strains were extracted at the outer skins (top and bottom faces) and their respective interfaces with the core. Processing this file allowed for the proper structuring of the matrix $[M]$ by rigorously associating the spatial coordinates $(x, z)$ with the corresponding acquired strain values, which allowing the solution of the inverse problem on an element-by-element. It is important to specify that the spatial domain analyzed in the *iFEM* environment extends for a length of $300mm$, exactly corresponding to the half effective span of the beam ($L_{eff}/2$), neglecting for simplicity of calculation the effect of the overhanging portion beyond the supports. For the **B1** beam (which will also be the subject of the subsequent experimental campaign), the *iFEM* algorithm was initially tested by simulating a discretization with 3 inverse elements. Consequently, 12 readings were extracted to compose the following matrix $[M]$, corresponding to 3 measurement stations centered at the longitudinal coordinated $x_{sen}$=`[95, 225, 280] mm`. These acquired values were

directly employed to construct the matrix $[M]$, associating the longitudinal readings with the specific transverse coordinates $z$ where the virtual sensors are located, as illustrated in the previous geometric schematic.

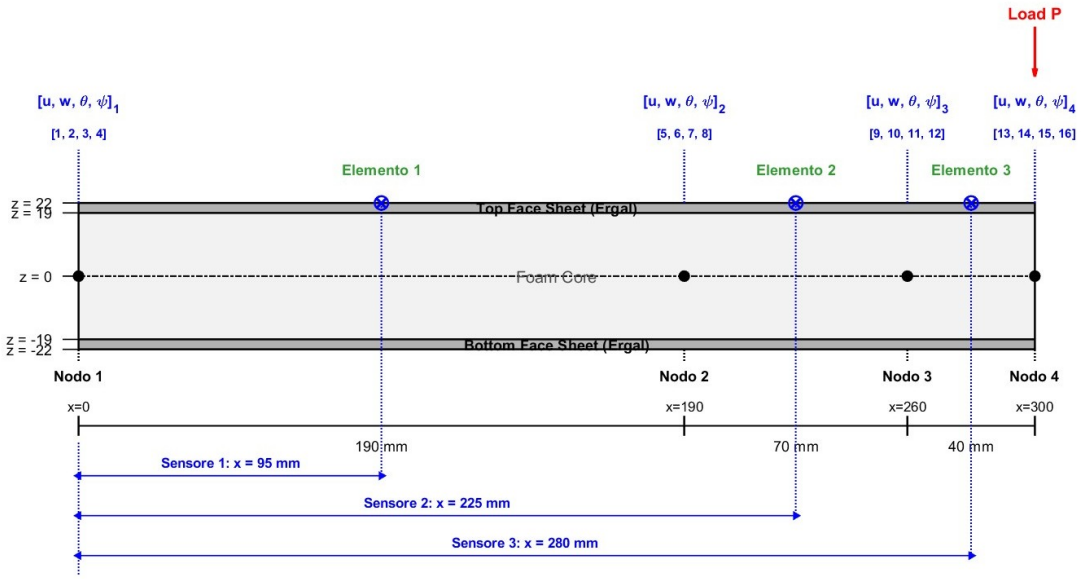


**Figure 4.5:** Sensors

As observed from the results reported in Table 4.3 this configuration proved to be insufficient. Although the enriched formulation ($e = 1$) manages to approximate the actual displacement calculated by Patran, the purely kinematic solution ($e = 0$) diverges drastically. Since in a convergent and structurally stable *iFEM* framework the two limiting cases must yield almost identical results, this wide discrepancy clearly indicates that a too sparce network (only 3 sensors) is unable to adequately capture the complex shear gradients typical of a sandwich panel. Consequently, to overcome this critical issue and ensure the convergence of the model, it was necessary to densify the acquisition network, moving from 3 to 6 sensors.

| Node | DOF | e = 0 | e = 1 |
|---|---|---|---|
| **Node 1** | $u_1$ [1] | -7.1280e-05 | -7.1280e-05 |
| | $w_1$ [2] | 0.0000e+00 | 0.0000e+00 |
| | $\theta_1$ [3] | 1.1774e-03 | 1.1774e-03 |
| | $\phi_1$ [4] | -1.9553e-03 | -1.6055e-02 |
| **Node 2** | $u_2$ [5] | -4.6580e-05 | -4.6580e-05 |
| | $w_2$ [6] | -6.5032e-01 | -1.7938e+00 |
| | $\theta_2$ [7] | 8.6028e-04 | 8.6028e-04 |
| | $\phi_2$ [8] | -2.8525e-03 | -7.9204e-04 |
| **Node 3** | $u_3$ [9] | -4.2100e-05 | -4.2100e-05 |
| | $w_3$ [10] | -8.8227e-01 | -2.3733e+00 |
| | $\theta_3$ [11] | 4.5028e-04 | 4.5028e-04 |
| | $\phi_3$ [12] | -2.4641e-03 | -1.4462e-02 |
| **Node 4** | $u_4$ [13] | 0.0000e+00 | 0.0000e+00 |
| | $w_4$ [14] | -9.4056e-01 | -2.6722e+00 |
| | $\theta_4$ [15] | 0.0000e+00 | 0.0000e+00 |
| | $\phi_4$ [16] | 0.0000e+00 | 0.0000e+00 |

**Table 4.3:** Nodal displacements

Nevertheless, it is worth nothing that despite the lack of convergence between the $e = 0$ and $e = 1$ cases the relative error between the *MSC Patran* model $-2.58mm$ and the enriched *iFEM* formulation ($e = 1$, resulting in $-2.6722mm$) remains relatively small, sitting at approximately 3.57%.

### 4.5.2 Sandwich beam B1 - six sensors

The transition to a six sensor configuration was implemented to increase the accuracy of the results, aiming to achieve full convergence between both $e = 0$ and $e = 1$ formulations, and with respect to the *MSC Patran* reference model. In this phase, the analysisi was still conducted by comparing the $320mm$ half-beam in *MSC Patran* (which includes the overhanging portion beyonf the support 4.3) with the $300mm$ effective in *MATLAB*.
To accommodate this new layout, the $300mm$ domain was discretized into **six inverse finite elements**, each equipped with simulated strain sensors exactly at its centers. The longitudinal coordinates of the sensors are $x_{sen}$ `= [40, 100, 165, 225, 250, 280] mm`. Since four strain readings at different transverse heights ($z$) were extracted for each longitudinal station, a total of 24 strain values were acquired to construct the expanded measurement matrix $[M]$ and feed the inverse solver.

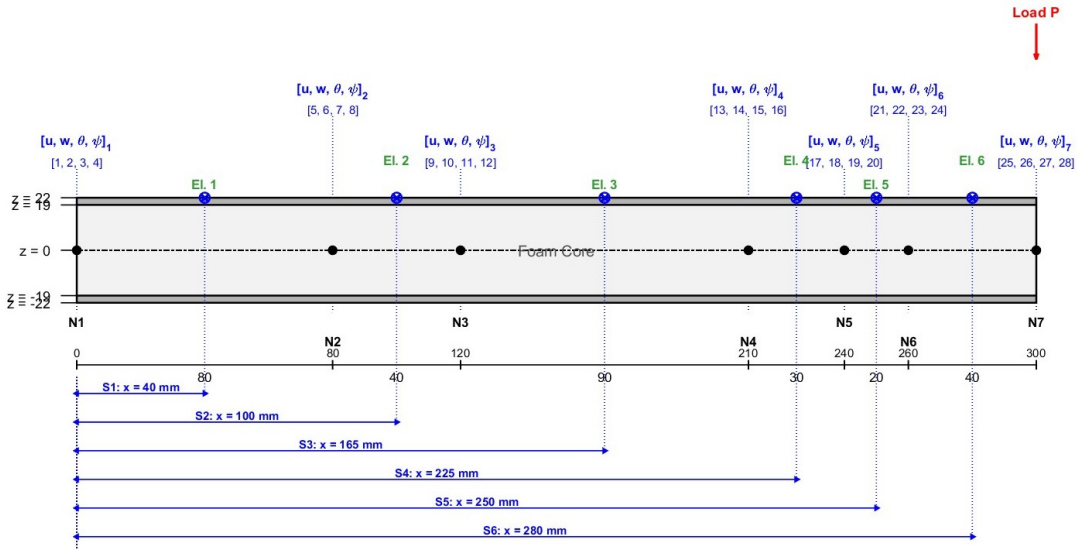


**Figure 4.6:** Schematic representation of the *iFEM* discretization using six inverse element

Once the $[M]$ matrix was populated and the transverse shear parameters ($\gamma$ and $\eta$) were analytically derived through the equilibrium equations, the nodal displacements were computed and summarized in Table 4.4. As can be clearly seen, the formulations $e = 0$ and $e = 1$ still do not converge with each other. However, the $e = 1$ case now converges exceptionally well with the *MSC Patran* model, registering a relative error of only about 0.7%. This is a highly positive outcome: increasing the number of sensors successfully improved the computational accuracy, confirming that this denser six sensor layout is reliable and will be adopted during the experimental phase.

| Node | DOF | e = 0 | e = 1 |
|---|---|---|---|
| **Node 1** | $u_1$ [1] | -1.1450e-04 | -1.1450e-04 |
| | $w_1$ [2] | 0.0000e+00 | 0.0000e+00 |
| | $\theta_1$ [3] | 9.4501e-04 | 9.4501e-04 |
| | $\phi_1$ [4] | 1.3584e-03 | -1.7750e-03 |
| **Node 2** | $u_2$ [5] | -5.4182e-05 | -5.4182e-05 |
| | $w_2$ [6] | -1.4439e-01 | -7.1737e-01 |
| | $\theta_2$ [7] | 1.1959e-03 | 1.1959e-03 |
| | $\phi_2$ [8] | -2.8272e-03 | -1.4022e-02 |
| **Node 3** | $u_3$ [9] | -5.0412e-05 | -5.0412e-05 |
| | $w_3$ [10] | -3.0685e-01 | -1.0778e+00 |
| | $\theta_3$ [11] | 1.1212e-03 | 1.1212e-03 |
| | $\phi_3$ [12] | -2.9788e-03 | -1.6617e-03 |
| **Node 4** | $u_4$ [13] | -5.0885e-05 | -5.0885e-05 |
| | $w_4$ [14] | -6.5939e-01 | -1.8729e+00 |
| | $\theta_4$ [15] | 7.7197e-04 | 7.7197e-04 |
| | $\phi_4$ [16] | -2.9624e-03 | -1.4155e-02 |
| **Node 5** | $u_5$ [17] | -4.8965e-05 | -4.8965e-05 |
| | $w_5$ [18] | -7.6629e-01 | -2.1261e+00 |
| | $\theta_5$ [19] | 5.9626e-04 | 5.9626e-04 |
| | $\phi_5$ [20] | -2.7960e-03 | -1.2875e-03 |
| **Node 6** | $u_6$ [21] | -4.2100e-05 | -4.2100e-05 |
| | $w_6$ [22] | -9.4056e-01 | -2.6722e+00 |
| | $\theta_6$ [23] | -8.2936e-01 | -2.2963e+00 |
| | $\phi_6$ [24] | 4.5028e-04 | 4.5028e-04 |
| **Node 7** | $u_7$ [25] | 0.0000e+00 | 0.0000e+00 |
| | $w_7$ [26] | -8.8765e-01 | -2.6074e+00 |
| | $\theta_7$ [27] | 0.0000e+00 | 0.0000e+00 |
| | $\phi_7$ [28] | 0.0000e+00 | 0.0000e+00 |

**Table 4.4:** Nodal displacements

Nevertheless, the persistent divergence between $e = 0$ and $e = 1$ suggests an underlying boundary issue. A strong hypothesis is that utilizing two geometrically completely different models, comparing a *Patran* beam with an overhang against a *MATLAB* beam without it, introduces a structural discrepancy that the internal equilibrium equations cannot resolve. Consequently, to definitively address this divergence, the following section will investigate a perfectly matched geometric configuration, modeling both environments identically (either with or without the overhanging portion $20mm$).

### 4.5.3 Implementation of the full-length model to resolve discrepancies

To definitively resolve the convergence issue between the $e = 0$ and $e = 1$ formulations, the geometric domains of *MSC Patran* and *MATLAB* were perfectly aligned. The total length of the half-beam was extended to $320mm$ in the *iFEM* code, thus explicty including the overhanging portion to the left of the support 4.3.
This geometric update required the addition of an extra inverse finite element, bringing to total to **seven elements**. Consequently, an additional virtual sensor was introduced at the center of this new element to ensure proper data acquisition along the overhang. The new **seven sensor** configuration is located at the longitudinal coordinates $x_{sen}$=`[10, 60, 120, 185, 245, 270, 300] mm`. To accomodate these additional reading, the measurement matrix $[M]$ was expanded to 28 rows, successfully feeding the updated inverse solver.

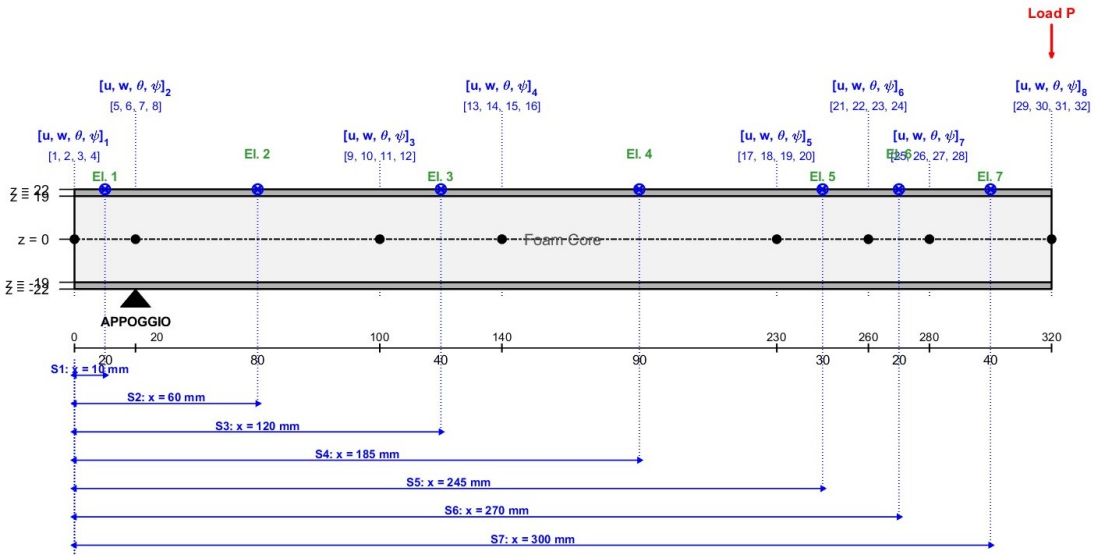


**Figure 4.7:** Schematic representation using seven inverse elements

The results obtained form this complete geometry model demonstrate a successful restoration of algorithmic convergence 4.5. Both the $e = 0$ and $e = 1$ formulations now align much more closely with each other and, most importantly, with the *MSC Patran* reference model. Specifically, the relative error for the $e = 0$ dropped to approximately 12% while the formulation enriched with the equilibrium equations $e = 1$ achieved a remarkable error of just 3%. This outcome confirms that matching the physical boundary conditions and the structural overhang was crucial for the stability of the model.

| Node | DOF | e = 0 | e = 1 |
|---|---|---|---|
| **Node 1** | $u_1$ [1] | -1.3454e-04 | -1.3454e-04 |
| | $w_1$ [2] | 1.2933e-01 | 1.7947e-01 |
| | $\theta_1$ [3] | 1.5142e-03 | 1.5142e-03 |
| | $\phi_1$ [4] | -4.4763e-03 | -1.1847e-02 |
| **Node 2** | $u_2$ [5] | -1.2407e-04 | -1.2407e-04 |
| | $w_2$ [6] | 0.0000e+00 | 0.0000e+00 |
| | $\theta_2$ [7] | 1.5769e-03 | 1.5769e-03 |
| | $\phi_2$ [8] | -5.3661e-03 | -2.9630e-03 |
| **Node 3** | $u_3$ [9] | -7.9130e-05 | -7.9130e-05 |
| | $w_3$ [10] | -6.2693e-01 | -7.3767e-01 |
| | $\theta_3$ [11] | 1.6143e-03 | 1.6143e-03 |
| | $\phi_3$ [12] | -7.1159e-03 | -1.2390e-02 |
| **Node 4** | $u_4$ [13] | -7.8460e-05 | -7.8460e-05 |
| | $w_4$ [14] | -9.7531e-01 | -1.0989e+00 |
| | $\theta_4$ [15] | 1.5119e-03 | 1.5119e-03 |
| | $\phi_4$ [16] | -7.1772e-03 | -2.4327e-03 |
| **Node 5** | $u_5$ [17] | -7.8235e-05 | -7.8235e-05 |
| | $w_5$ [18] | -1.7357e+00 | -1.9168e+00 |
| | $\theta_5$ [19] | 1.1103e-03 | 1.1103e-03 |
| | $\phi_5$ [20] | -7.0989e-03 | -1.3251e-02 |
| **Node 6** | $u_6$ [21] | -7.0435e-05 | -7.0435e-05 |
| | $w_6$ [22] | -1.9729e+00 | -2.1734e+00 |
| | $\theta_6$ [23] | 9.0222e-04 | 9.0222e-04 |
| | $\phi_6$ [24] | -6.6990e-03 | -1.6839e-03 |
| **Node 7** | $u_7$ [25] | -5.4670e-05 | -5.4670e-05 |
| | $w_7$ [26] | -2.1151e+00 | -2.3491e+00 |
| | $\theta_7$ [27] | 7.1306e-04 | 7.1306e-04 |
| | $\phi_7$ [28] | -5.9035e-03 | -1.4525e-02 |
| **Node 8** | $u_8$ [29] | 0.0000e+00 | 0.0000e+00 |
| | $w_8$ [30] | -2.2474e+00 | -2.6605e+00 |
| | $\theta_8$ [31] | 0.0000e+00 | 0.0000e+00 |
| | $\phi_8$ [32] | 0.0000e+00 | 0.0000e+00 |

**Table 4.5:** Nodal displacements

### 4.5.4 Implementation of the overhang-free configuration

Having confirmed that matching the spatial domains between *MSC Patran* and *MATLAB* successfully restores the convergence of the results, the same rationale was applied to model the **B1** beam by considering only its effective length of

300$mm$. Performing the static analysis in *MSC Patran* the deformation field shown in Figure 4.8.

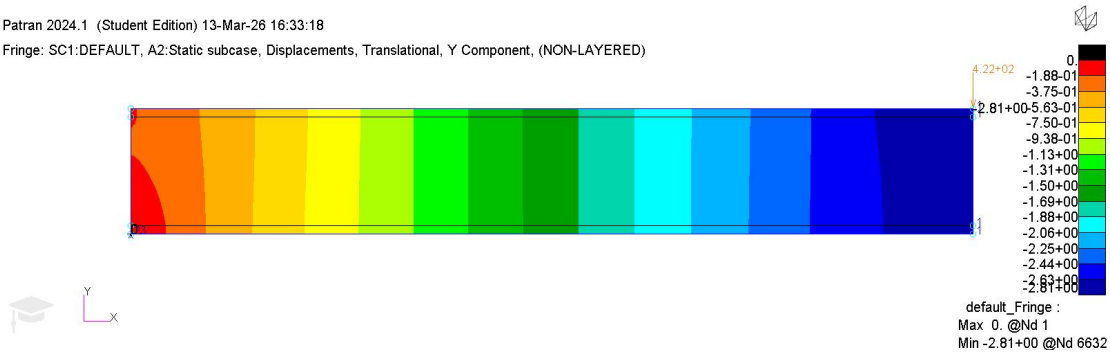


**Figure 4.8:** Displacement overhang-free configuration

As previously discussed, the primary focus is on deflection at the loaded cross-section, which exhibits a local peak value of $-2.81mm$ and a minimum of $-2.73mm$. Averaging these through-thickness values results in an equivalent transverse displacement of $-2.77mm$. This average value serves as the reference numerical target for the comparison with the *iFEM* model.

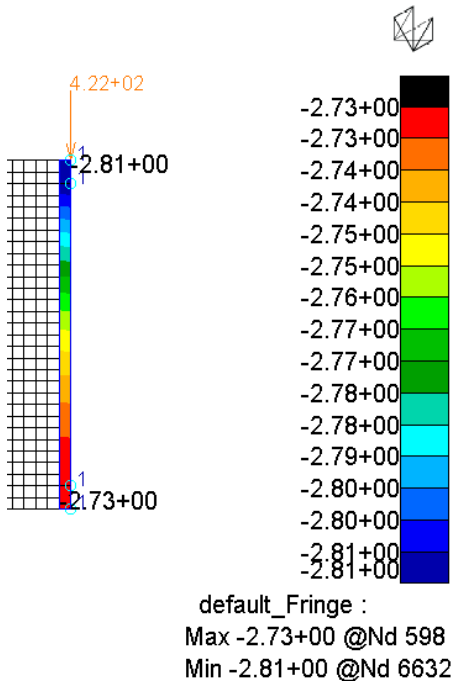


**Figure 4.9:** Detail of the transverse displacement (y-component)

For this configuration, the set up consists of the six sensors located at the same longitudinal coordinates used previously $x_{sen}$ `= [40, 100, 165, 225, 250, 280] mm` 4.6. This specific layout is fundamentally driven by the upcoming experimental phase, where strain gauges will not installed on the overhanging portion to the left of the support. To run the inverse analysis, a total of 24 strain readings (four transverse heights for each of the six longitudinal stations) were extraced from the Patran results to construct the measurement matrix $[M]$, successfully feeding the inverse solver.
The results summized in Table 4.6 are obtained by implementing the updated matrix $[M]$ and equilibrium equations in the *iFEM* code.
Once again, a strong trend toward convergence between the $e = 0$ and $e = 1$ formulations is observed. Although they do not yield perfectly identical values, both provide physically consistent and comparable results with respect to the direct *FEM* analysis. Specifically, $e = 0$ results in a relative error of approximately 13.4%, while $e = 1$ achieves an outstanding relative error of just 1.1%.

| Node | DOF | e = 0 | e = 1 |
|---|---|---|---|
| **Node 1** | $u_1$ [1] | -1.7873e-04 | -1.7873e-04 |
| | $w_1$ [2] | 0.0000e+00 | 0.0000e+00 |
| | $\theta_1$ [3] | 1.8181e-03 | 1.8181e-03 |
| | $\phi_1$ [4] | -8.7989e-03 | -3.7418e-03 |
| **Node 2** | $u_2$ [5] | -7.7650e-05 | -7.7650e-05 |
| | $w_2$ [6] | -7.7965e-01 | -8.3708e-01 |
| | $\theta_2$ [7] | 1.6237e-03 | 1.6237e-03 |
| | $\phi_2$ [8] | -7.2506e-03 | -1.3752e-02 |
| **Node 3** | $u_3$ [9] | -7.8610e-05 | -7.8610e-05 |
| | $w_3$ [10] | -1.1313e+00 | -1.2306e+00 |
| | $\theta_3$ [11] | 1.5130e-03 | 1.5130e-03 |
| | $\phi_3$ [12] | -7.1932e-03 | -2.7696e-03 |
| **Node 4** | $u_4$ [13] | -7.8160e-05 | -7.8160e-05 |
| | $w_4$ [14] | -1.8925e+00 | -2.0544e+00 |
| | $\theta_4$ [15] | 1.1104e-03 | 1.1104e-03 |
| | $\phi_4$ [16] | -7.0993e-03 | -1.2952e-02 |
| **Node 5** | $u_5$ [17] | -7.0435e-05 | -7.0435e-05 |
| | $w_5$ [18] | -2.1296e+00 | -2.3034e+00 |
| | $\theta_5$ [19] | 9.0225e-04 | 9.0225e-04 |
| | $\phi_5$ [20] | -6.6993e-03 | -1.5676e-03 |
| **Node 6** | $u_6$ [21] | -5.4670e-05 | -5.4670e-05 |
| | $w_6$ [22] | -2.2718e+00 | -2.4659e+00 |
| | $\theta_6$ [23] | 7.1306e-04 | 7.1306e-04 |
| | $\phi_6$ [24] | -5.9035e-03 | -1.3222e-02 |
| **Node 7** | $u_7$ [25] | 0.0000e+00 | 0.0000e+00 |
| | $w_7$ [26] | -2.4042e+00 | -2.7491e+00 |
| | $\theta_7$ [27] | 0.0000e+00 | 0.0000e+00 |
| | $\phi_7$ [28] | 0.0000e+00 | 0.0000e+00 |

**Table 4.6:** Nodal displacements

In conclusion, this section has comprehensively demonstrated that adopting inconsistent geometric domains between the *iFEM* and *Patran* models leads to unreliable and inaccurate estimations. Conversely, perfectly matching the beam's dimensions and optimizing the sensor network guarantees high-fidelity reconstructions. It is crucial to emphasize that the number of sensors was deliberately capped at six within this specific layout. Introducing an excessive number of sensors, particularly too close to the load application points or the supports, would trigger sever numerical oscillations due to local stress concentrations, ultimately degrading the stability and accuracy of the entire inverse reconstruction.

### 4.5.5 Implementation of the penalty technique for the overhanging domain

As highlighted in the previous numerical tests, using a direct *Patran* model that includes the structural overhang alongside an inverse *MATLAB* model that excludes it leads to a critical failure of the $e = 0$, while the $e = 1$ demonstrates better resilience. Consequently, a definitive methodological solution was required to model the entire extended beam without deploying additional physical strain gauges on the overhanging portion.

To achieve this, a specific penalization strategy was introduced: the *MATLAB* domain was extended to include the overhang by adding a seventh inverse element 4.7. To conserve sensors, it was assumed that the deformations in this specific overhanging region are negligible. Consequently, the measures for this extra element were arbitrarily set to zero, which subsequently causes the known right-hand side vectors ($\{b_u\}$, $\{b_\theta\}$, $\{b_\phi\}$, $\{b_\eta\}$, $\{b_\gamma\}$) to vanish.

To prevent this zero-strain information from corrupting the overall inverse reconstruction if slightly inaccurate, $\alpha = 10^{-4}$ was applied to the entire structural contribution of the seventh element. Specifically, all local assembly matrices for this overhanging element ($[A_u]$, $[A_\theta]$, $[A_\phi]$, and for $e = 1$, also $[A_\eta]$ and $[A_\gamma]$) are pre-multiplied by this penalty factor. This ensurer that the global weight of this artificial element remains strictly negligible, allowing the algorithm to run stably without being heavily constrained by the zero-strain assumption.

By implementing this modified penalized assembly, the inverse analysis yielded the nodal displacements reported in Table 4.7

| Node | DOF | e = 0 | e = 1 |
|---|---|---|---|
| **Node 1** | $u_1$ [1] | -1.2407e-04 | -1.2407e-04 |
| | $w_1$ [2] | 1.3886e-01 | 3.2018e-02 |
| | $\theta_1$ [3] | 1.5769e-03 | 1.5769e-03 |
| | $\phi_1$ [4] | -5.3661e-03 | 2.3634e-03 |
| **Node 2** | $u_2$ [5] | -1.2407e-04 | -1.2407e-04 |
| | $w_2$ [6] | 0.0000e+00 | 0.0000e+00 |
| | $\theta_2$ [7] | 1.5769e-03 | 1.5769e-03 |
| | $\phi_2$ [8] | -5.3661e-03 | -2.4354e-03 |
| **Node 3** | $u_3$ [9] | -7.9130e-05 | -7.9130e-05 |
| | $w_3$ [10] | -6.2693e-01 | -7.9936e-01 |
| | $\theta_3$ [11] | 1.6143e-03 | 1.6143e-03 |
| | $\phi_3$ [12] | -7.1159e-03 | -1.4316e-02 |
| **Node 4** | $u_4$ [13] | -7.8460e-05 | -7.8460e-05 |
| | $w_4$ [14] | -9.7531e-01 | -1.1870e+00 |
| | $\theta_4$ [15] | 1.5119e-03 | 1.5119e-03 |
| | $\phi_4$ [16] | -7.1772e-03 | -1.9679e-03 |
| **Node 5** | $u_5$ [17] | -7.8235e-05 | -7.8235e-05 |
| | $w_5$ [18] | -1.7357e+00 | -2.0003e+00 |
| | $\theta_5$ [19] | 1.1103e-03 | 1.1103e-03 |
| | $\phi_5$ [20] | -7.0989e-03 | -1.3477e-02 |
| **Node 6** | $u_6$ [21] | -7.0435e-05 | -7.0435e-05 |
| | $w_6$ [22] | -1.9729e+00 | -2.2517e+00 |
| | $\theta_6$ [23] | 9.0222e-04 | 9.0222e-04 |
| | $\phi_6$ [24] | -6.6990e-03 | -1.2467e-03 |
| **Node 7** | $u_7$ [25] | -5.4670e-05 | -5.4670e-05 |
| | $w_7$ [26] | -2.1151e+00 | -2.4152e+00 |
| | $\theta_7$ [27] | 7.1306e-04 | 7.1306e-04 |
| | $\phi_7$ [28] | -5.9035e-03 | -1.3598e-02 |
| **Node 8** | $u_8$ [29] | 0.0000e+00 | 0.0000e+00 |
| | $w_8$ [30] | -2.2474e+00 | -2.7052e+00 |
| | $\theta_8$ [31] | 0.0000e+00 | 0.0000e+00 |
| | $\phi_8$ [32] | 0.0000e+00 | 0.0000e+00 |

**Table 4.7:** Nodal displacements

As evident from the extracted data, the proposed numerical trick effectively prevents the algorithm from completely diverging when faced with misaligned geometries. Extracting the maximum deflection at the loaded node (Node 8), the $e = 1$ formulation calculates a displacement of $-2.70mm$, resulting in a highly satisfying relative error of approximately 4.8% compared to the *Patran* target ($-2.58mm$).

On the other hand, the $e = 0$ formulation predicts a maximum deflection of $-2.24mm$, which translates to an error of nearly 12.9%.

## 4.6 Sandwich beam B2

Following the comprehensive analysis of beam **B1**, which was also experimentally investigated, the study progressed to the **B2** sandwich beam. Thanks to the session file automation capabilities in *MSC Patran*, the set up process for this new geometry was significantly accelerated. Beam **B2** differs from the previuos configuration primarily in its total length, which is $490mm$ and its total thickness, which is $43.3mm$, as detailed in Table 4.2. Since the specific configuration was not subjected to laboratory testing, a simulated concentrated load of $-10000N$ was applied to the half-beam model. Based the unpromising results obtained for the **B1** beam with sparse sensor networks, configurations with fewer than six sensor were excluded a priori for **B2**. Instead, the primary expectation for this initial test is that the geometric mismatch caused by the structural overhang will once again prevent convergence between the formulations $e = 0$ and $e = 1$. Accordingly, the first numerical test compares an *MSC Patran* model that includes the overhang (half total length = $245mm$) against a *MATLAB iFEM* model strictly limited to the effective span ($225mm$).

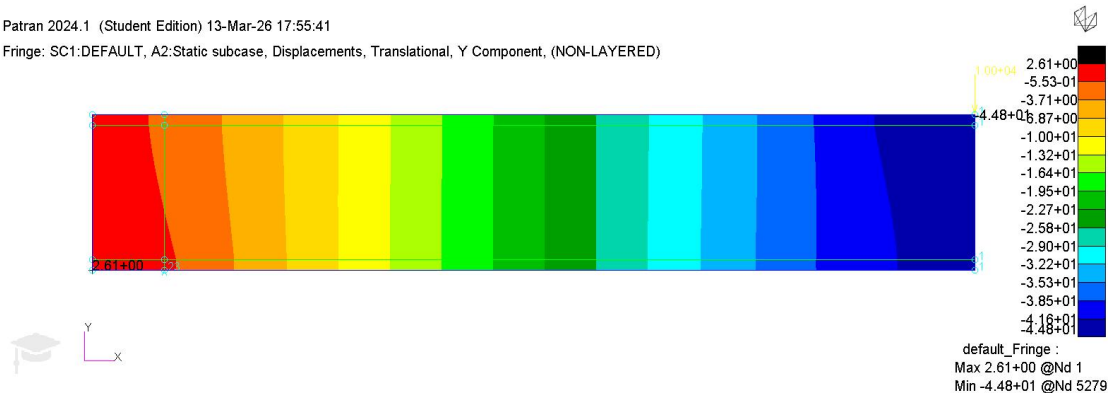


**Figure 4.10:** Displacement

As depicted in the subsequent detailed view 4.11, the static analysis in *MSC Patran* environment has a maximum deflection of $-44.8mm$ at the point of application of the force and a minimum of $-42.8mm$, in an average transverse displacement of $-43.8mm$, which serves as the exact reference ground truth for the *iFEM* comparison.

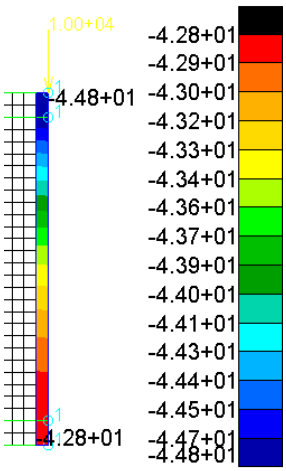


**Figure 4.11:** Detail of the y-displacement of beam b2

Longitudinal strains $\epsilon_{xx}$ were subsequently extracted at the core interfaces and the outer skins to construct the measurement matrix $[M]$. Note that $z-coordinates$ differs from the **B1** case due to the increase in total thickness of beam **B2**. Located the virtual sensors at $x_{sen}$ `= [35, 87.5, 120, 150, 175, 205] mm` 4.12, the 24 rows matrix was assembled to feed the inverse solver.

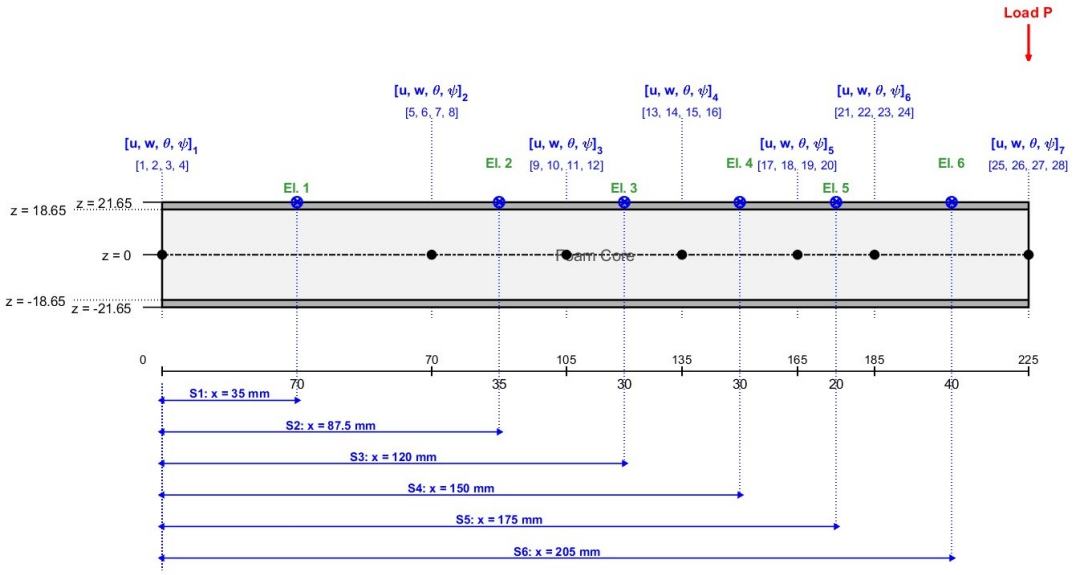


**Figure 4.12:** Schematic representation of the *iFEM* discretization for the B2

By implementing this updated matrix and the equilibrium equations within the *iFEM* code, the results summarized in Table 4.8 are obtained. Consistent with

the previous finding, the geometric discrepancy between *Patran* and *MATLAB* prevents the convergence between $e = 0$ and $e = 1$. Nevertheless, $e = 1$ successfully approximates the *Patran* reference, calculating a maximum deflection of $-44.4mm$. This corresponds to a highly satisfactory relative error of approximately 1.4%. Consequently, to fully restore algorithmic convergence for the **B2** beam, the subsequent analyses will enforce perfectly matched geometric domains between *MSC Patran* and *MATLAB*, investigating both the fully extended length (with overhang) and the strictly effective span (without overhang).

| **Node** | **DOF** | **e = 0** | **e = 1** |
|---|---|---|---|
| **Node 1** | $u_1$ [1] | -2.5287e-03 | -2.5287e-03 |
| | $w_1$ [2] | 0.0000e+00 | 0.0000e+00 |
| | $\theta_1$ [3] | 1.0949e-02 | 1.0949e-02 |
| | $\phi_1$ [4] | 4.2367e-02 | -5.1405e-02 |
| **Node 2** | $u_2$ [5] | -1.2687e-03 | -1.2687e-03 |
| | $w_2$ [6] | -1.8969e+00 | -1.3985e+01 |
| | $\theta_2$ [7] | 1.8185e-02 | 1.8185e-02 |
| | $\phi_2$ [8] | -6.7429e-02 | -3.1912e-01 |
| **Node 3** | $u_3$ [9] | -1.1226e-03 | -1.1226e-03 |
| | $w_3$ [10] | -4.9677e+00 | -2.1068e+01 |
| | $\theta_3$ [11] | 1.6989e-02 | 1.6989e-02 |
| | $\phi_3$ [12] | -7.2874e-02 | -7.2874e-02 |
| **Node 4** | $u_4$ [13] | -1.1234e-03 | -1.1234e-03 |
| | $w_4$ [14] | -7.6340e+00 | -2.7160e+01 |
| | $\theta_4$ [15] | 1.4972e-02 | 1.4972e-02 |
| | $\phi_4$ [16] | -7.2917e-02 | -3.2600e-01 |
| **Node 5** | $u_5$ [17] | -1.0949e-03 | -1.0949e-03 |
| | $w_5$ [18] | -1.0168e+01 | -3.3046e+01 |
| | $\theta_5$ [19] | 1.2060e-02 | 1.2060e-02 |
| | $\phi_5$ [20] | -6.8962e-02 | -3.6494e-02 |
| **Node 6** | $u_6$ [21] | -9.4800e-04 | -9.4800e-04 |
| | $w_6$ [22] | -1.1678e+01 | -3.7076e+01 |
| | $\theta_6$ [23] | 9.3725e-03 | 9.3725e-03 |
| | $\phi_6$ [24] | -6.0667e-02 | -3.5024e-01 |
| **Node 7** | $u_7$ [25] | 0.0000e+00 | 0.0000e+00 |
| | $w_7$ [26] | -1.3079e+01 | -4.4410e+01 |
| | $\theta_7$ [27] | 0.0000e+00 | 0.0000e+00 |
| | $\phi_7$ [28] | 0.0000e+00 | 0.0000e+00 |

**Table 4.8:** B2 Nodal displacements

### 4.6.1 Implementation of the full-length B2 model to resolve discrepancies

As demonstrated in the previous section, the geometric mismatch between the modeled domains in *MSC Patran* and *MATLAB* hindered the accuracy of the inverse reconstruction. To resolve this, the analysis of beam **B2** now proceeds by modeling the exact same domain length in both environments. The entails explicitly including the overhanging portion beyond the support, resulting in a modeled half-length of $245mm$. Under this perfectly matched configuration, the reference *Patran* static analysis provides a displacement of $-43.8mm$ 4.10.
To accommodate this extended domain in *MATLAB*, an additional inverse finite element was introduced over the overhang, requiring the installation of extra virtual sensors at its center. The seven sensor array updated is located at the longitudinal coordinates $x_{sen}$ `= [35, 87.5, 120, 150, 175, 205, 235] mm`.

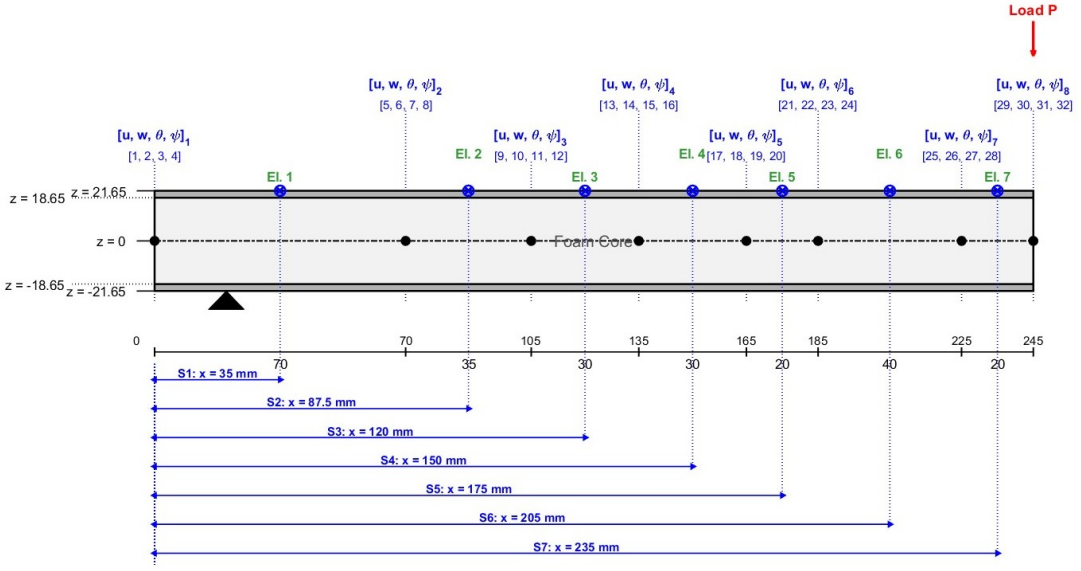


**Figure 4.13:** Schematic representation of the iFEM discretization for the full-length B2

Based on the strain data extracted from the *Patran* model at these station, the expanded 28 rows measurement matrix $[M]$ was assembled to feed the algotithm. Guaranteeing an exact geometric match allows the *iFEM* results to highlight a regained convergence between $e = 0$ and $e = 1$ formulations. Moreover, the displacement fields converge toward the reference *MSC Patran* model with significantly higher accuracy. However, an interesting shift in relative errors is observed compared to beam **B1**: $e = 0$ achieves a highly accurate relative error of 4.8%, while $e = 1$ has a slightly higher error of 13.9%. This seems counterintuitive results

was largely anticipated, the beam **B2** is characterized by a lower span-to-thickness ratio than the previously analyzed beam **B1**.

| **Node** | **DOF** | **e = 0** | **e = 1** |
|---|---|---|---|
| **Node 1** | $u_1$ [1] | -3.1907e-03 | -3.1907e-03 |
| | $w_1$ [2] | 0.0000e+00 | 0.0000e+00 |
| | $\theta_1$ [3] | 2.1781e-02 | 2.1781e-02 |
| | $\phi_1$ [4] | -6.7284e-02 | -3.0399e-01 |
| **Node 2** | $u_2$ [5] | -1.9307e-03 | -1.9307e-03 |
| | $w_2$ [6] | -1.0331e+01 | -1.5918e+01 |
| | $\theta_2$ [7] | 2.9017e-02 | 2.9017e-02 |
| | $\phi_2$ [8] | -1.7708e-01 | -9.9965e-02 |
| **Node 3** | $u_3$ [9] | -1.7846e-03 | -1.7846e-03 |
| | $w_3$ [10] | -1.7619e+01 | -2.3568e+01 |
| | $\theta_3$ [11] | 2.7821e-02 | 2.7821e-02 |
| | $\phi_3$ [12] | -1.8253e-01 | -2.8090e-01 |
| **Node 4** | $u_4$ [13] | -1.7854e-03 | -1.7854e-03 |
| | $w_4$ [14] | -2.3899e+01 | -2.9789e+01 |
| | $\theta_4$ [15] | 2.5804e-02 | 2.5804e-02 |
| | $\phi_4$ [16] | -1.8257e-01 | -7.8965e-02 |
| **Node 5** | $u_5$ [17] | -1.7569e-03 | -1.7569e-03 |
| | $w_5$ [18] | -3.0047e+01 | -3.5825e+01 |
| | $\theta_5$ [19] | 2.2892e-02 | 2.2892e-02 |
| | $\phi_5$ [20] | -1.7861e-01 | -2.7692e-01 |
| **Node 6** | $u_6$ [21] | -1.6100e-03 | -1.6100e-03 |
| | $w_6$ [22] | -3.3968e+01 | -3.9556e+01 |
| | $\theta_6$ [23] | 2.0205e-02 | 2.0205e-02 |
| | $\phi_6$ [24] | -1.7032e-01 | -4.9324e-02 |
| **Node 7** | $u_7$ [25] | -6.6200e-04 | -6.6200e-04 |
| | $w_7$ [26] | -4.0188e+01 | -4.6848e+01 |
| | $\theta_7$ [27] | 1.0832e-02 | 1.0832e-02 |
| | $\phi_7$ [28] | -1.0965e-01 | -2.8931e-01 |
| **Node 8** | $u_8$ [29] | 0.0000e+00 | 0.0000e+00 |
| | $w_8$ [30] | -4.1393e+01 | -4.9915e+01 |
| | $\theta_8$ [31] | 0.0000e+00 | 0.0000e+00 |
| | $\phi_8$ [32] | 0.0000e+00 | 0.0000e+00 |

**Table 4.9:** B2 Nodal displacements

Ultimately, it can be concluded that the value most accurately approximating the *Patran* reference model is the one computed using $e = 0$, while $e = 1$ has

an excessively high displacement value, confirming its tendency to significantly overestimate the global deformation in structures characterized by this specific stockiness.

### 4.6.2 Implementation of the overhang-free B2 configuration

In light of the overestimation observed in the previous configuration, the modeling of beam **B2** proceeded by removing the overhanging portion beyond the support. Thus, the spatial domain was strictly reduced to the effective span of $225mm$ in both computation environments.
This static analysis conducted in *MSC Patran* has a maximum displacement of $-49.3mm$ and minimum of $-42.7mm$ at the load application node, resulting in average deflection of approximately $-46mm$. This value was adopted as the exact ground truth for the validation of the inverse algorithm.

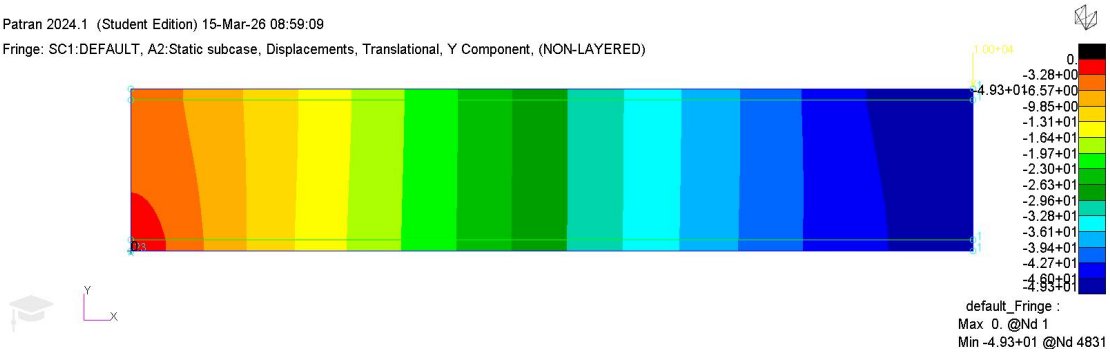


**Figure 4.14:** Displacement overhang-free B2 configuration

Having reduced the domain length, the sensor network reverted to the six element configuration positioned at the geometric centers, with longitudinal coordinates $x_{sen}$ `= [35, 87.5, 120, 150, 175, 205] mm` 4.12. By extracting the $\epsilon_{xx}$ strain from *Patran* model at the specific coordinates, the following 24 row measurement matrix $[M]$ was assembled. By providing this matrix as input to the *iFEM* code, the calculated results, summarized in Table 4.10 depict a highly positive outcome. As is evident from the data. A decisive convergence is restored between the $e = 0$ and $e = 1$ formulations, both of which align very satisfactorily with the reference *FEM* model.

| Node | DOF | e = 0 | e = 1 |
|---|---|---|---|
| **Node 1** | $u_1$ [1] | -4.1438e-03 | -4.1438e-03 |
| | $w_1$ [2] | 0.0000e+00 | 0.0000e+00 |
| | $\theta_1$ [3] | 3.2832e-02 | 3.2832e-02 |
| | $\phi_1$ [4] | -2.1803e-01 | -1.2149e-01 |
| **Node 2** | $u_2$ [5] | -1.8040e-03 | -1.8040e-03 |
| | $w_2$ [6] | -1.6048e+01 | -1.7233e+01 |
| | $\theta_2$ [7] | 2.8369e-02 | 2.8369e-02 |
| | $\phi_2$ [8] | -1.7929e-01 | -3.0991e-01 |
| **Node 3** | $u_3$ [9] | -1.8047e-03 | -1.8047e-03 |
| | $w_3$ [10] | -2.3228e+01 | -2.5071e+01 |
| | $\theta_3$ [11] | 2.6104e-02 | 2.6104e-02 |
| | $\phi_3$ [12] | -1.7649e-01 | -8.2980e-02 |
| **Node 4** | $u_4$ [13] | -1.8122e-03 | -1.8122e-03 |
| | $w_4$ [14] | -2.9218e+01 | -3.1434e+01 |
| | $\theta_4$ [15] | 2.3447e-02 | 2.3447e-02 |
| | $\phi_4$ [16] | -1.7327e-01 | -2.9310e-01 |
| **Node 5** | $u_5$ [17] | -1.6547e-03 | -1.6547e-03 |
| | $w_5$ [18] | -3.4909e+01 | -3.7275e+01 |
| | $\theta_5$ [19] | 1.9677e-02 | 1.9677e-02 |
| | $\phi_5$ [20] | -1.6303e-01 | -5.0759e-02 |
| **Node 6** | $u_6$ [21] | -1.2970e-03 | -1.2970e-03 |
| | $w_6$ [22] | -3.8328e+01 | -4.1051e+01 |
| | $\theta_6$ [23] | 1.5889e-02 | 1.5889e-02 |
| | $\phi_6$ [24] | -1.4325e-01 | -2.9548e-01 |
| **Node 7** | $u_7$ [25] | 0.0000e+00 | 0.0000e+00 |
| | $w_7$ [26] | -4.1510e+01 | -4.7395e+01 |
| | $\theta_7$ [27] | 0.0000e+00 | 0.0000e+00 |
| | $\phi_7$ [28] | 0.0000e+00 | 0.0000e+00 |

**Table 4.10:** B2 nodal displacements

Specifically, $e = 0$ exhibits a relative error of 10.8%, while $e = 1$ registers an outstanding error of 2.7%. The latter represents a significant improvement compared to 13.9% obtained in the overhang configuration.

## 4.7 Summary and conclusions of the numerical tests

To offer a clear big-picture view of the numerical simulations conducted so far, Table 4.11 summarizes the maximum deflections obtained from both *Patran* and the *iFEM* algorithm. Specifically, this comparison allows us to fully appreciate the real impact that the choice of the geometric domain has on the final results for the **B1** and **B2** beams.

| Beam | Patran Domain (FEM) | MATLAB Domain (iFEM) | Patran Target | $w_{max}$ (e=0) | Error (e=0) | $w_{max}$ (e=1) | Error (e=1) |
|---|---|---|---|---|---|---|---|
| **B1** | With overhang (320 mm) | W/o overhang (300 mm) | -2.58 mm | -0.89 mm | 65.5 % | -2.61 mm | 0.7 % |
| **B1** | With overhang (320 mm) | With overhang (320 mm) | -2.58 mm | -2.25 mm | 12.9 % | -2.66 mm | 3.0 % |
| **B1** | With overhang (320 mm) | Penalized overhang | -2.58 mm | -2.25 mm | 12.9 % | -2.71 mm | 4.8 % |
| **B1** | W/o overhang (300 mm) | W/o overhang (300 mm) | -2.77 mm | -2.40 mm | 13.4 % | -2.75 mm | 1.1 % |
| **B2** | With overhang (245 mm) | W/o overhang (225 mm) | -43.80 mm | -13.08 mm | 70.1 % | -44.41 mm | 1.4 % |
| **B2** | With overhang (245 mm) | With overhang (245 mm) | -43.80 mm | -41.39 mm | 4.8 % | -49.92 mm | 13.9 % |
| **B2** | W/o overhang (225 mm) | W/o overhang (225 mm) | -46.00 mm | -41.51 mm | 10.8 % | -47.40 mm | 2.7 % |

**Table 4.11:** Summary of the maximum deflections and relative errors for beams B1 and B2 under various geometric configurations.

As can be seen from the data, misaligned configurations (where the *Patran* half-beam includes the overhang while the *iFEM* discretization lacks it) lead to critical instabilities and severe underestimations in the $e = 0$ formulation. Conversely, when identical geometric domains are set in both environments, an immediate and drastic reduction in the error is observed precisely for the $e = 0$ formulation, demonstrating how spatial alignment is the key factor in restoring the global consistency of the model.
Conversely, it is worth noting that the $e = 1$ formulation demonstrates a remarkable robustness to these boundary differences. Even in completely mismatched set ups, the $e = 1$ formulation successfully compensates for the missing structural information, maintaining excellent accuracy and yielding relative error as low as 0.7% for the **B1** beam and 1.4% for the **B2** beam.

# Chapter 5

# Experimental assessment

This chapter concerns the implementation and validation of the *iFEM* model developed in *MATLAB* environment applied to the experimental case.
After demonstrating the theorical and numerical robustness of the algorithm through comparison with models in *MSC Patran*, it is essential to validate the code in a real-world scenario. Indeed, the application to experimental data represents the ultimate testing ground for the *iFEM* technology, as it introduces all the typical complexities of the physical world that a purely numerical model tends to idealize.

## 5.1 Test structure and system

The three-point bending experimental test was conducted at the **LAQ-AERMEC Aeromechanical Structural Systems laboratory** of the *Department of Mechanical and Aerospace Engineering of Politecnico di Torino*. The test was performed on the **B1** sandwich beam, whose geometry and costituent material properties were previously introduced and summarized in 4.1 and 4.2. During the execution of the test, the beam was placed on two semi-cylindrical supports and subjected to a concentrated load at the center of the beam.

**Load cell** The load is applied through a loading bridge, which is coupled with an **S-type load cell** (specifically, the *Tedea-Huntleigh model 516 in nickel-plated steel*). This cell operates via an integrated balanced strain gauge bridge circuit, enabling it to act as a transducer to measure the intensity of the force applied to the structure with high precision.
The force is generated by the rotation of a loading mechanism, which induces a controlled displacement of the loading system towards the beam. This mechanism allows for the application of a controlled load into the cell, ensuring precision in the measurements. Furthermore, to ensure that the force vector remains strictly

vertical with respect to the plane of the beam, the load cell is designed with a typical **S** geometry characterized by two opposite cutouts, figure 5.1.


**Figure 5.1:** S-type load cell

This structural conformation provides the cell with excellent stability and allows it to compensate for any misalignments, significantly improving the accuracy and reliability of the measurement. [12]

**Strain gauge** For the acquisition of the measurement of the local strains experienced by the structure during the test, a network of *uniaxial electrical resistance strain gauge*, characterized by a nominal resistence of *120 ohm*, was employed. As is well known, the strain gauge is a resistive transducer consisting of a thin conductive metallic grid, which is the sensing element, deposited on a flexible polymeric backing.

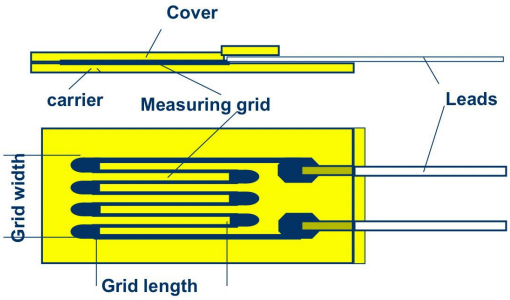


**Figure 5.2:** Strain Gauge [13]

The characteristic folded geometry of the grid specifically designed to maximize the sensor's sensitivity along the primary measurement axis while simultaneously keeping its overall dimensions extremely compact. The operating principle is based on the **piezoresistive effect**: as the structure bend under the action of the applied load, the deformation is fully transmitted to the polymeric backing and, consequently, to the metallic grid.
The elongation of the latter causes a change in its cross-sectional area and length, generating a proportional variation in the electical resistence of the circuit. [13]
As discussed in the previuos chapter the test configuration and the beam geometry exhibit perfect symmetry with respect to the midspan section. By exploitinf this structural and loading symmetry, the kinematic and deformative behaviour of the entire domain can be accurately studied and reconstructed by analyzing only one half of it. For this reason, the experimental set up was optimized by concentrating the installation of the the strain gauge network exclusively on one of the two halves of the beam. Specifically, the sensors were posizioned parallel to the longitudinal axis and structurally attached to both the upper 5.4 and lower faces 5.3 of the outer skins.

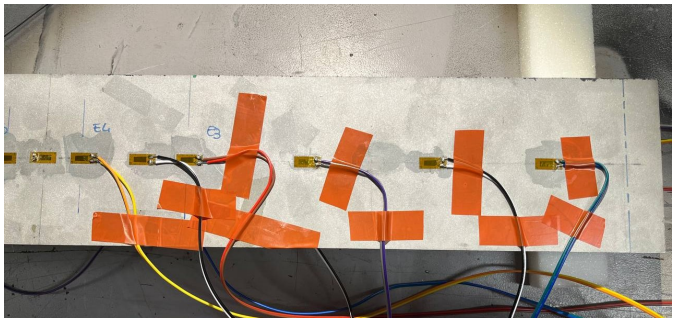

**Figure 5.3:** Lower face

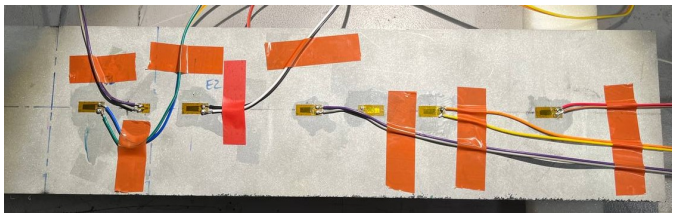

**Figure 5.4:** Upper face

This strategic arrangement allows for a complete mapping of the flexural strain field of the half-beam: the resistance variation, appropriately conditioned and recorded by the data acquisition system, indeed makes it possible to punctually derive the

longitudinal strains ($\epsilon_{xx}$).
As illustrated in the following schematic 5.5, a total of 12 real strain gauges are physically installed on the beam. They are positioned in pairs, bonded to the top and bottom skins across the six designated measurement stations, the numbering of these sensors has been arranged in reverse order, counting backwards from the loaded free end ($x = 320mm$) toward the support.

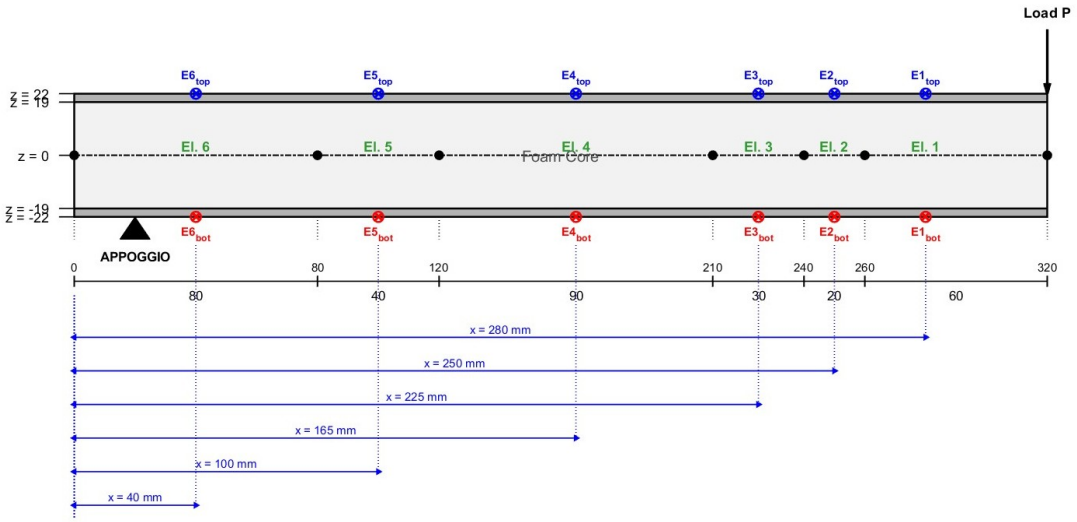


**Figure 5.5:** Schematic representation of the experimental setup

**Fibre optic sensors** To complement and enrich the localized measurements provided by the strain gauge network, the experimental campaign employed an advanced structural health monitoring tecnology based on *Distributed fibre optic sensors (DFOS)* [11]. Specifically, high-definition strain sensors (*HD strain sensors*) were utilized, interrogated by means of **Luna ODiSI 6000 series** system. Unlike traditional discrete sensors, the ODiSI system allows to acquisition of thousands of strain measurements per meter of a single high-definition fibre optic sensor, ensuring an ultra-high resolution mapping. [14]
From a construction standpoint, the HD sensors employed consist of a *polymide coated low bend fiber*. Thanks to their extremely reduced diameter, equal to $155\mu m$, and their flexibility, these fibres are minimally invasive [15]. This feature allowed the direct integration of the optical sensors within the structure embedded, positioning them in the sandwich layup to directly measure the axial strain at the interfaces. [11]
Regarding the installation layout, the single fiber optic cable was laid at the sandwich interfaces following a specific serpentine path, figure 5.6.

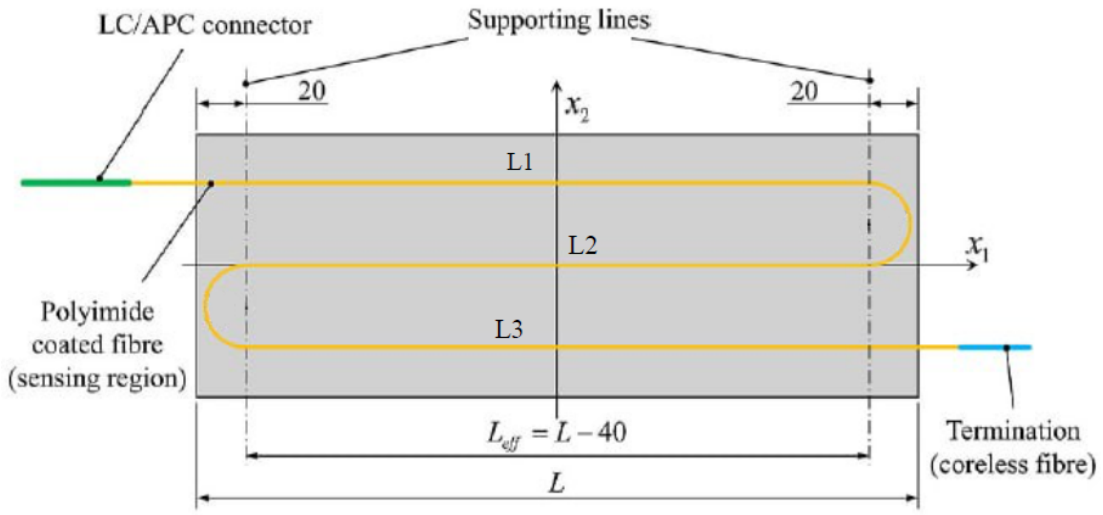


**Figure 5.6:** HD strain sensors [11]

Exploiting the remarkable flexibility of sensor, the fibre was shaped by making U turns in order to create three straight segments, identified ad **L1, L2** and **L3**, oriented parallel to longitudinal axis of the beam. [11]
The choice of having three measurement lines (L1, L2 and L3) on the same interface instead of just one is of fundamental importance from a data processing perspective. Fibre optic sensors, indeed, possess such a high spatial resolution that they are extremely sensitive to local geometric micro-imperfection. By spatially avaraging the strains read along the three straight paths, it was possible to obtain a single longitudinal strain function, cleaned of local disturbances and highly representative of the actual global flexural behavior of the beam. [11]

## 5.2 Experimental procedure

The three-point bending test was carried out under static conditions, with the force gradually applied until a maximum of roughly $-86.09kg$ was attained. The time history of the applied force measured by the load cell is illustrated in Figure 5.7, presenting the loading phase followed by the unloading stage.
Following the definition of the experimental set up, the preparatory phase of the test required the physical installation of the sensors. To faithfully reproduce the numerical model, the strain gauges were positioned on the exact same portion of the beam analyzed in *Patran*, replicating the longitudinal coordinates previously optimized within the *MATLAB* environment. Specifically, the six sensor layout was adopted, having been identified as the optimal configuration to ensure stable,

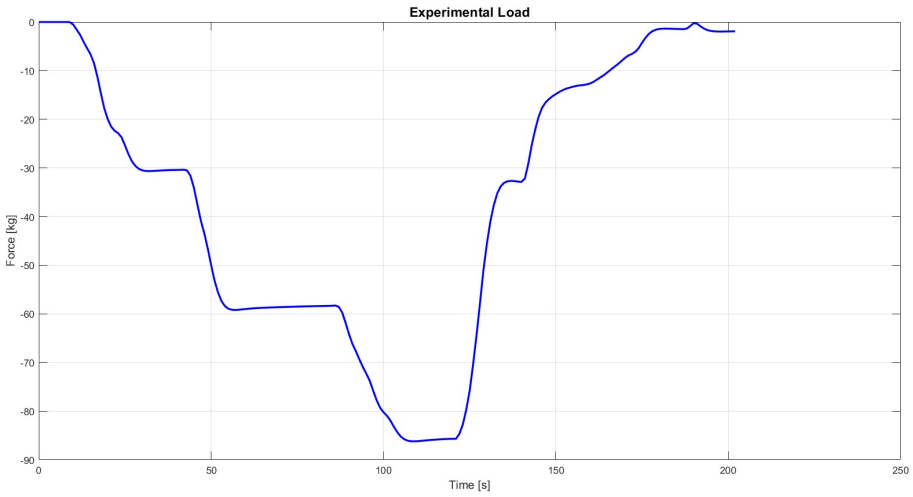


**Figure 5.7:** Experimental load

convergent results that are highly representative of the structure's actual physical behavior.
From an operational standpoint, the strain gauges were bonded using a fast-curing adhesive: this ensured perfect structural cohesion and the accurate transfer of strains across both the upper and lower faces. Following the bonding process, the electrical terminals were soldered, and the corresponding wiring cables were routed and connected to the data acquisition system.
In addition to monitoring local strains, to precisely measure the beam's deflection and verify the load application, symmetrically, and without any unwanted rigid body motions, the experimental set up was equipped with the inductive displacement transducers (LVDT - Linear Variable Differential Transformers) [1].
As can be observed in the figure 5.8, the measurement instruments were positioned on both the right and left sides of the beam to ensure symmetry with respect to the applied load. This specific arrangement was implemented exclusively to record the magnitude of the displacement and subsequently calculate its average, with the objective of highlighting any potential misalignments during load application.

[1]These are inductive sensors, which means that displacement is measured based on the current induced by the sliding of the plunger, have a measurement range of $5mm$, and it is recommended to operate them at the midpoint of this range for optimal performance [13]

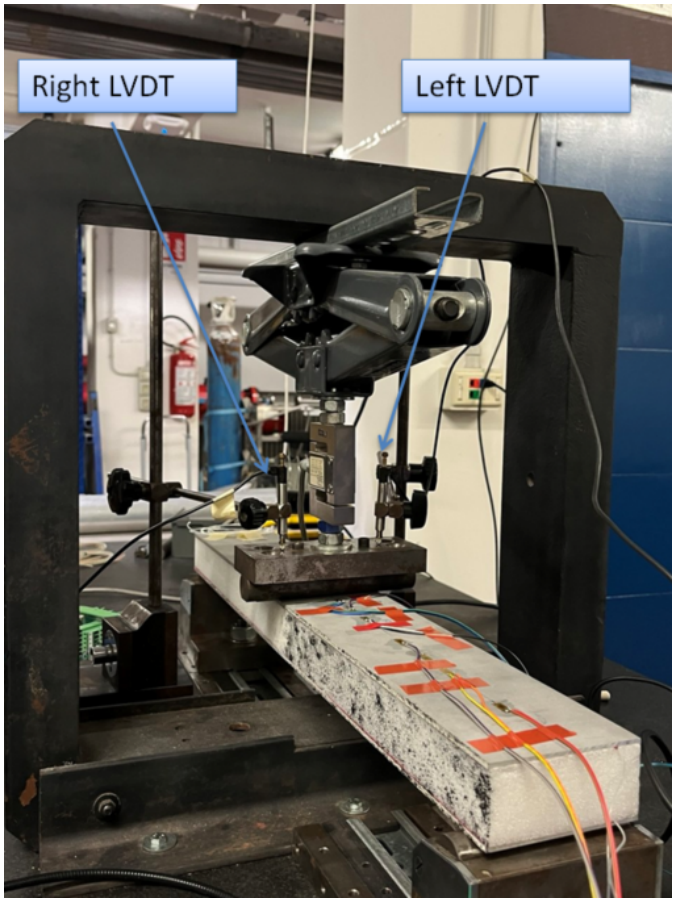


**Figure 5.8:** LVDT

To ensure a comprehensive characterization of the beam's structural response, the monitoring phase relied on the integration of two independent acquisition systems, each optimized for the specific sensing technologies employed.
The acquisition of discrete resistive data was handled by the **HBM MGCplus** device. This system was dedicated exclusively to the twelve strain gauge, located on the upper 5.4 and lower face 5.3, which guaranties a stable and uninterrupted recording of signals at a sampling frequency of $1Hz$.
The figure below illustrates the time history of the local deformations acquired by the stain gauge network 5.9.
In parallel, the **Luna ODiSI 6000** system was employed to map the continuous strain field via distributed fiber optic sensors (DFOS). This technology enabled the high-definition interrogation of the fibers with a spatial resolution of $1.3mm$ and a frequency of $1.04Hz$, capturing the detailed strain distribution along the sandwich interfaces.
The integration of this technology represents a fundamental added value compared

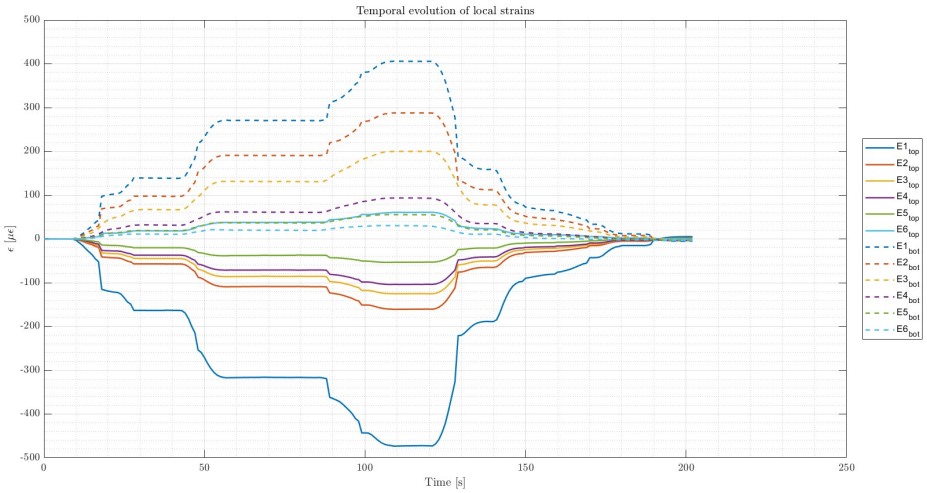


**Figure 5.9:** Temporal evolution of local strains

to the traditional strain gauge network, because strain gauge provide purely discrete and local readings, while the fiber optic sensors return a continuous strain profile along the entire longitudinal extent of the structure. From an operational standpoint, the acquisition system was configured utilizing two independent optical channels: the **first channel** was dedicated to the continuous monitoring of the **upper face**, while the **second channel** recorded the strains on the **lower face**.
The hybrid experimental approach proved to be decisive for the implementation of the *iFEM* formulation. Having access to the data acquired via *DFOS* allows the inverse algorithm to be fed not only with discrete readings but also with a continuous strain field featuring an extremely high spatial density along the entire extent of the structure. From an analytical perspective, the countinuous strain profiles thus obtained will be temporally synchronized with the reading from the strain gauge network and the load cell data, allowing for the extraction and analysis of the exact strain field corresponding to the maximum load achieved during the test.

## 5.3 Experimental validation of the numerical model

The experimental validation of theoretical and numerical models represents a fundamental methodological step. This section presents a direct comparison between the maximum displacement obtained from the finite element analysis and the one actually measured during the test.
At the maximum load of $-86.09kg$, the average reading recorded an experimental

deflection of $-3.16mm$. Concurrently, by converting this load into *Newton* and applying half of it to the *Patran FEM model*, exploiting the symmetry conditions illustrated in the previous chapter, the analysis yielded an average displacement of $-2.56mm$. The comparison between the real and numerical data reveals a relative error of approximately 18.99%.
The fact that the displacement predicted by *Patran* is lower than the real one indicates that the numerical model is globally stiffer than the physical structure. This behavior is highly justifiable: the *FEM* environment represents an ideal condition, characterized by perfectly rigid boundary conditions, homogeneous material and a total absence of defects. In the real case, while the inevitable physiological compliance of the support, the micro-settlements of the beam during load application and the manufacturing tolerances of the sandwich panel naturally contribute to increasing the overall flexibility of the measured system.
It is precisely in light of these unavoidable kinematic discrepancies between set up that the power of the *iFEM* approach emerges. By relying on the strain field actually measured by the strain gauges and fiber optics, the inverse formulation allows for bypassing the need to define external loading condition, which are often uncertain or difficult to model in operational environments, thus reconstructing the actual displacement field with a significantly higher degree of fidelity.

## 5.4 Implementation and validation of the iFEM approach

This section represents the methodological and operational core of the thesis, in which the experimentally acquired data are processed to feed the *iFEM* formulation. The numerical approach adopted faithfully follows the one validated in the previous chapters: the computational domain was discretized using six inverse elements, positioning the virtual sensors in the center of the elements, corresponding to exact same coordinates $x$ as the physical sensors: $x_{sen}$ `= [40, 100, 165, 225, 250, 280] mm`.
From a geometric point of view using the symmetry of the bending setup, the numerical processing was restricted to the **half-beam** comprised between the midspan and the support, for an effective length of $300mm$. The portion of material protruding beyond the constraint was deliberately excluded from the*iFEM* domain, as it is an unloaded area, devoid of instrumentation, and therefore irrelevant for the purposes of kinematic reconstruction.
The most delicate step for the initialization of the inverse algorithm is the construction of the strain input matrix $[M]$. Since the strain gauge control unit and the fiber optic interrogator system, *Luna ODiSI*, operate on different time bases and sampling frequencies, a rigorous signal synchronization was necessary. Both

datasets were aligned by extracting the strain values at the exact instant when the load cell recorded the maximum force peak.

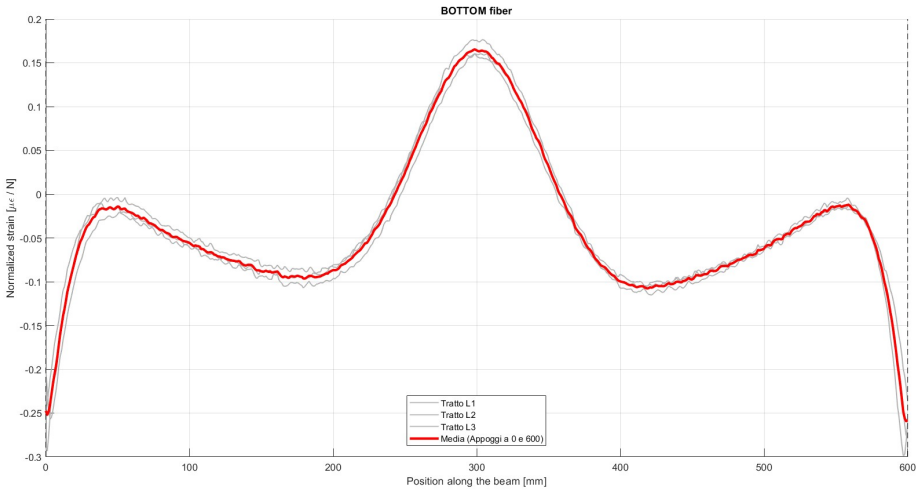


**Figure 5.10:** Peak strain on the bottom surface

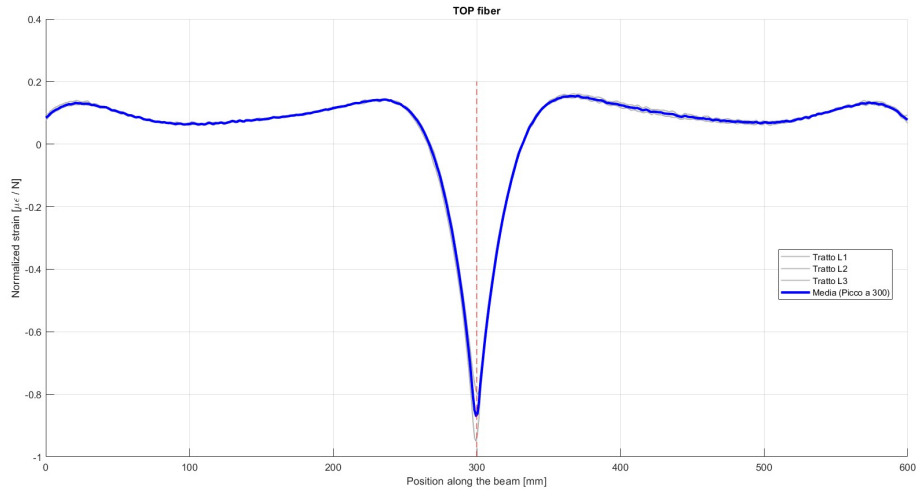


**Figure 5.11:** Peak strain on the top surface

Furthermore, a specific spatial post-processing was dedicated to the fiber optic data. Since the latter was bonded following a serpentine path, with three longitudinal passes along the beam 5.6, the three strain profiles were isolated, realigned to compensate for the return segments, and finally averaged mathematically. This

operation ensured the extraction of an extremely robust continuous strain profile, filtered from any local noise. Subsequently, the continuous readings from the fiber were interpolated at the precise longitudinal coordinates of the strain gauges. In this way, the final matrix $[M]$ collects and maps the strain along the entire thickness of the sandwich panel at six different longitudinal stations, interrogating four distinct elevations: the upper strain gauges and the upper branch of the fiber and the lower branch of the fiber and the lower strain gauges.
Following the time synchronization and spatial post-processing operations described above, the strain input matrix for the algorithm consists of the 24 rows, corresponding to the strain readings collected across the six longitudinal measurement stations.
The specific vertical positions ($z$ coordinates) of the strain gauges at each station, along with the overall sensor layout used to populate the measurement matrix $[M]$ at the instant of maximum experimental load, are illustrated in Figure 5.5.
Analyzing the values, it cleary emerges how the *iFEM* approach allows for approximating the actual physical behavior of the structure with a significantly higher degree of fidelity compared to the traditional *FEM*. As previously highlighted, the experimentally measured maximum deflection was $-3.16mm$, while the *iFEM* algorithm, processing the sensor data, reconstructed a maximum displacement of $-2.76mm$ in $e = 0$ and $-2.94mm$ in $e = 1$.
These results translate to relative error of 12.66% for the $e = 0$ case and only 6.96% for the $e = 1$ case. The evident improvement associated with $e = 1$ confirms the necessity of including the shear deformability of the core for an accurate modeling of sandwich materials.

| **Node** | **DOF** | **e = 0** | **e = 1** |
|---|---|---|---|
| **Node 1** | $u_1$ [1] | -6.6154e-04 | -6.6154e-04 |
| | $w_1$ [2] | 0.0000e+00 | 0.0000e+00 |
| | $\theta_1$ [3] | 1.6494e-03 | 1.6494e-03 |
| | $\phi_1$ [4] | -8.1199e-03 | 8.6979e-03 |
| **Node 2** | $u_2$ [5] | -7.5350e-06 | -7.5350e-06 |
| | $w_2$ [6] | -8.3713e-01 | -4.7194e-01 |
| | $\theta_2$ [7] | 1.7039e-03 | 1.7039e-03 |
| | $\phi_2$ [8] | -9.4550e-03 | -1.7153e-02 |
| **Node 3** | $u_3$ [9] | -2.7695e-05 | -2.7695e-05 |
| | $w_3$ [10] | -1.2781e+00 | -7.9966e-01 |
| | $\theta_3$ [11] | 1.6064e-03 | 1.6064e-03 |
| | $\phi_3$ [12] | -9.2811e-03 | 4.1172e-03 |
| **Node 4** | $u_4$ [13] | -2.0207e-04 | -2.0207e-04 |
| | $w_4$ [14] | -2.1955e+00 | -1.7558e+00 |
| | $\theta_4$ [15] | 1.2079e-03 | 1.2079e-03 |
| | $\phi_4$ [16] | -8.2922e-03 | -2.2626e-02 |
| **Node 5** | $u_5$ [17] | 1.1710e-05 | 1.1710e-05 |
| | $w_5$ [18] | -2.4644e+00 | -2.1300e+00 |
| | $\theta_5$ [19] | 9.8917e-04 | 9.8917e-04 |
| | $\phi_5$ [20] | 9.8917e-04 | 3.4853e-06 |
| **Node 6** | $u_6$ [21] | 2.5070e-04 | 2.5070e-04 |
| | $w_6$ [22] | -2.6199e+00 | -2.4039e+00 |
| | $\theta_6$ [23] | 7.8811e-04 | 7.8811e-04 |
| | $\phi_6$ [24] | -6.3384e-03 | -2.5928e-02 |
| **Node 7** | $u_7$ [25] | 0.0000e+00 | 0.0000e+00 |
| | $w_7$ [26] | -2.7624e+00 | -2.9476e+00 |
| | $\theta_7$ [27] | 0.0000e+00 | 0.0000e+00 |
| | $\phi_7$ [28] | 0.0000e+00 | 0.0000e+00 |

**Table 5.1:** Experimental nodal displacements

The residual 6.96% deviation from the experimental data is entirely physiological and is fully justifiable by practical and environmental factors intrinsic to the the test setup. These include possible slight asymmetries in the supports and in the load application with respect to the midplane, positioning tolerances of the instrumentation, and the inevitable background noise present in the signals acquired by the sensors during the execution of the test.
As previously anticipated, one of the primary causes underlying this residual deviation can be attributed to a physiological misalignment during the load application. This asymmetry is not a theoretical hypothesis but finds objective confirmation in

the experimental data acquired by the two LVDT positioned respectively on the right and left sides of the beam at midspan 5.8. Analyzing the trend of the two readings, a clear divergence in deflection becomes evident as the load increases: the left side of the structure consistently records higher displacement values compared to the right side.

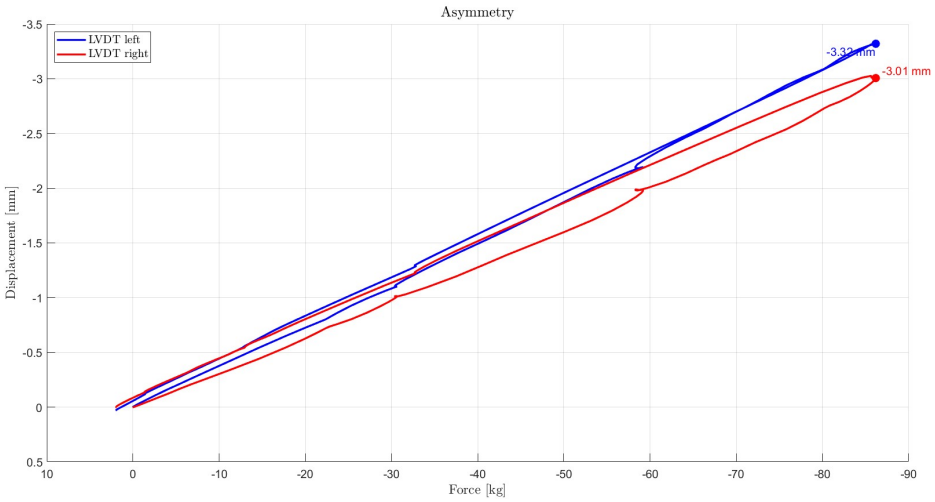


**Figure 5.12:** Asymmetry

This evidence points to an uneven load distribution between the left and right sides of the beam is clearly reflected in the distributed strain profiles acquired by the fiber optic sensors 5.13 and 5.14. Recalling that the *DFOS* sensors was bonded following a serpentine path with three longitudinal passes, it can be observed that the **L1** measurement line (on the left side) consistently exihibits higher strain levels than the **L3** line (on the right side).

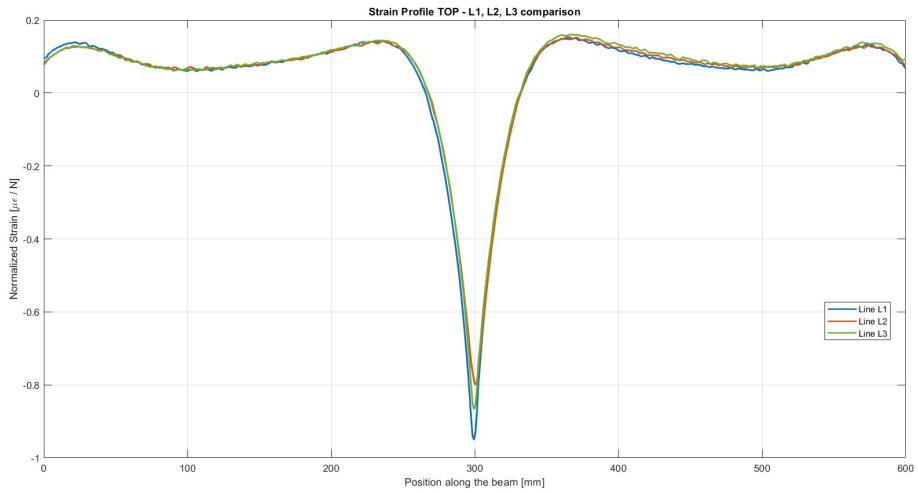


**Figure 5.13:** Strain profile TOP

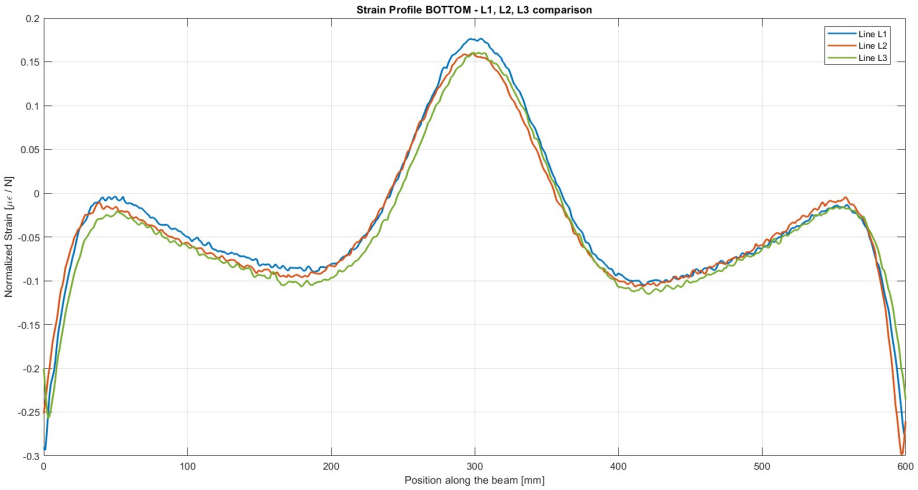


**Figure 5.14:** Strain profile BOTTOM

In conclusion, by combining the data from the LVDTs and the fiber optic sensors, it was possible to discover a practical issue during the test: the load was not applied uniformly to the beam. While the contact was perfect on the left side, the loading element did not properly touch the surface on the right. The fact that both show the same difference between the two sides confirms this asymmetry.
This evidence justifies the 6.96% deviation observed in the *iFEM* model, which confirms the high sensitivity and reliability of the entire measurement systems.

The ability of the instrumentation to precisely detect and quantify even these experimental imperfections adds further value to the validation of the inverse model, demonstrating its robustness even in the presence of the real non-idealized loading conditions.

# Chapter 6

# Conclusions

This thesis work aimed to develop and validate a one-dimensional inverse finite element for the structural health monitoring (*shape sensing*) of sandwich beams. The core idea was to combine the versatility of the **inverse Finite Element Method (iFEM)** with the kinematic precision of the **Refined Zigzag Theory (RZT)**. This approach allowed overcoming the classical theoretical limitations in modeling the complex stress and strain states typical of composite materials.
The algorithm, which was entirely developed in the *MATLAB* environment, was designed to reconstruct the entire displacement field starting from simple discrete strain readings. To achieve this, two distinct resolution strategies were explored: a purely kinematic approach ($e = 0$) and a more advanced formulation ($e = 1$) which, by integrating the cross-sectional equilibrium equations, analytically derives the transverse shear components (average and zigzag) that surface sensors cannot directly measure.
The numerical comparison with high-fidelity models created in *MSC Patran* led to crucial methological:

- It was observed that the baseline formulation ($e = 0$) is extremely sensitive to geometric alignment. To avoid numerical divergences, it is essential to ensure a perfect overlap between the domain of the direct model and the inverse one, explicity modeling even the overhanging portions.
- Conversely, the $e = 1$ formulation demonstrated remarkable mathematical robustness. Even when operating in not perfectly aligned geometries, the algorithm maintained high physical consistency. In optimized configurations, it provided excellent reconstructions, reducing the relative error compared to the direct model ro values between 1% and 3% for different beam architectures (**B1** and **B2**)

The most significant achievement of the research was the experimental validation through a three-point bending test. The use of a hybrid sensor network, composed

of traditional electrical strain gauges and distributed fiber optic sensors (DFOS), allowed mapping the strain field with unprecedented spatial detail. As often happens in physical setups, the experimental data revealed physiological imperfections, such as a slight asymmetry in the load application. Despite the introduction of these non-ideal dynamics and the typical instrumental background noise, the code demonstrated remarkable reliability. Data processing confirmed the clear superiority of the $e = 1$ formulation, which is capable of reconstructing the maximum deflection with an error of just 6.96%.

A scientific aspect of particular relevance that emerged during the tests concerns precisely the different sensitivity of the algorithm to geometric mismatch. In the purely numerical comparison, omitting an overhanging portion generates a mathematical violation of the boundary conditions, forcing the algorithm to work on incompatible domains. In the experimental case, however, this critically is drastically mitigated: the sensors record the real physical strain, which already includes the global effect of the structure and the actual compliance of the constraints. Exploiting the least-squares formulation, the *iFEM* algorithm acts as an advanced filter, smoothly integrating the experimental data and bypassing the rigidity of theoretical models. This confirms the strong engineering vocation of the method, capable of adapting to the imperfections of operational environments.

In light of the obtained results, clear starting point emerge for future developments of this research. Firstly, it will be fundamental to systematically solve the problem of geometric alignment between the analytical and numerical configurations. A targeted investigation into the modeling techniques within *MSC Patran*, aimed at reproducing with absolute fidelity the stiffness of the supports and the actual boundary conditions, would allow for further reduction of the residual error percentages.

Furthermore, future efforts could focus on extending the current one-dimensional formulation towards two-dimensional finite elements (plates and shells), making the code intrinsically immune to boundary discontinuities. This step will allow applying the *shape sensing* technology to aerospace structures of complex topology, laying concrete foundations for the realization of fully operational *Digital Twins* in real flight scenarios.

# Bibliography


[1] A. Tessler K. Adnan and O. Erkan. «An enhanced inverse finite element method for displacement and stress monitoring of multilayered composite and sandwich structure». In: *International Journal of Solids and Structures* 110–111 (2017), pp. 310–332. DOI: 10.1016/j.ijsolstr.2017.02.006 (cit. on pp. 1–4, 7).

[2] Priscilla Cerracchio, M. Gherlone, M. Di Sciuva, and Alexander Tessler. «A novel approach for displacement and stress monitoring of sandwich structures based on the inverse Finite Element Method». In: *Composite Structures* 127 (2015), pp. 69–76. DOI: 10.1016/j.compstruct.2015.03.014 (cit. on pp. 1, 4, 5, 7).

[3] E. Zappino. *Sandwich Materials*. Lecture notes from course: Tecnologie Aerospaziali. 2025 (cit. on p. 2).

[4] Brischetto. *Modellazione numerica*. Lecture notes from course: Strutture Aeronautiche. 2025 (cit. on p. 3).

[5] Alexander Tessler, Marco Di Sciuva, and Marco Gherlone. «A refined zigzag beam theory for composite and sandwich beams». In: *Journal of Composite Materials* 43.9 (2009), pp. 1051–1081. DOI: 10.1177/0021998308097730 (cit. on pp. 5, 6).

[6] P. Savino, M. Gherlone, and F. Tondolo. «Shape sensing with inverse Finite Element Method for slender structures». In: *Structural Engineering and Mechanics* 72.2 (2019), pp. 217–227. DOI: 10.12989/sem.2019.72.2.217 (cit. on p. 5).

[7] Marco Gherlone, Alexander Tessler, and Marco Di Sciuva. «C0 beam elements based on the Refined Zigzag Theory for multilayered composite and sandwich laminates». In: *Composite Structures* 93.11 (2011), pp. 2882–2894. DOI: 10.1016/j.compstruct.2011.05.015 (cit. on pp. 10, 11).

[8] M. Gherlone. *Il metodo degli elementi finiti*. Lecture notes from course: Strutture Aeronautiche. 2024 (cit. on p. 21).

[9] Hexagon. *Patran 2025.2 Reference Manual*. 2025 (cit. on p. 30).

[10] E. Cestino. *Modellazione Parametrica mediante File Sessione*. Lecture notes from course: Analisi FEM. 2025 (cit. on p. 31).

[11] M. Sorrent and M. Gherlone. «Numerical and experimental predictions of the static behaviour of thick sandwich beams using a mixed 3,2-RZT formulation». In: *Finite elements in analysis and design* 242 (2024), p. 104267. DOI: 10.1016/j.finel.2024.104267 (cit. on pp. 31–33, 59, 60).

[12] *Tedea-Huntleigh*. Product Datasheet. Model 615 S-Type Load Cells (cit. on p. 57).

[13] G. Frulla. *Estensimetria*. Lecture notes from course: Sperimenrazione su strutture aerospaziali. 2025 (cit. on pp. 57, 58, 61).

[14] *Luna Innovations*. Datasheet. ODiSI 6000 series: optical distributed sensor interrogators (cit. on p. 59).

[15] *Luna Innovations*. Datasheet. HD strain sensors (cit. on p. 59).

# Acknowledgements

Al Professor Gherlone, la cui competenza è stata il punto di riferimento fondamentale di questa tesi. Grazie per aver messo a disposizione la sua esperienza e per aver dato la direzione giusta a ogni fase dello studio.

All'Ing. Esposito, per il contributo concreto e per aver seguito con attenzione lo sviluppo pratico del lavoro.